LBL-23593
UC-814

Lawrence Berkeley Laboratory
UNIVERSITY OF CALIFORNIA

EARTH SCIENCES DIVISION

Preliminary Capillary Hystersis Simulations for Fractured Rocks—Model Development and Results of Simulations

A. Niemi and G.S. Bodvarsson

November 1991

| LOAN COPY |
|Circulates |
|for 4 weeks| Bldg. 50 Library.
Copy 2
LBL-23593

Prepared for the U.S. Department of Energy under Contract Number DE-AC03-76SF00098

DISCLAIMER

This document was prepared as an account of work sponsored by the United States Government. While this document is believed to contain correct information, neither the United States Government nor any agency thereof, nor the Regents of the University of California, nor any of their employees, makes any warranty, express or implied, or assumes any legal responsibility for the accuracy, completeness, or usefulness of any information, apparatus, product, or process disclosed, or represents that its use would not infringe privately owned rights. Reference herein to any specific commercial product, process, or service by its trade name, trademark, manufacturer, or otherwise, does not necessarily constitute or imply its endorsement, recommendation, or favoring by the United States Government or any agency thereof, or the Regents of the University of California. The views and opinions of authors expressed herein do not necessarily state or reflect those of the United States Government or any agency thereof or the Regents of the University of California.

LBL-23593

Preliminary Capillary Hysteresis Simulations for Fractured Rocks—Model Development and Results of Simulations

A. Niemi and G. S. Bodvarsson

Earth Sciences Division
Lawrence Berkeley Laboratory
University of California
Berkeley, California 94720

November 1991

This work was carried out under U.S. Department of Energy Contract No. DE-AC03-76SF00098, administered by the DOE-Nevada Office, in cooperation with the U.S. Geological Survey, Denver.

Table of Contents

List of Figures v
List of Tables vii
Abstract ix
Acknowledgement xi

1.0. Introduction 1
2.0. Background on Hysteresis 3
  2.1. Measurements 5
  2.2. Models 7
3.0. Development of Hysteresis Models Used 9
  3.1. Interpolation from First-Order Scanning Curves (Model (1)) 9
  3.2. Empirical Model using the Interpolation Functions (Model (2)) 10
  3.3. Model using the Dependent Domain Theory (Model (3)) 14
4.0. Test Simulations with Models (1) and (2) 19
  4.1. System Modeled 19
  4.2. Simulations and Results 22
5.0. Capillary Hysteresis Simulations for a Fractured Rock under Variable Infiltration Conditions 27
  5.1. System Modeled 27
  5.2. Hysteresis Data 31
  5.3. Simulations with Model (1) (Ten-Year Cycle) 36
  5.4. Simulations with Model (2) (Ten-Year Cycle) 46
  5.5. Simulations with Model (3) (Ten-Year Cycle) 55
  5.6. Simulations with One-Year Cycle 64
6.0. Summary and Conclusions 69
7.0. References 73

List of Figures

		Page
Figure 1.	Examples of hypothetical hysteretic paths.	4
Figure 2.	Example of the "pumping effect" (Klute and Heermann, 1974 and Jaynes, 1984).	6
Figure 3.	Example of scanning paths generated with model (2).	12
Figure 4.	Parameters for scanning paths with model (3).	16
Figure 5a.	Discretized flow region used in the test simulations.	20
Figure 5b.	Hypothetical hysteresis data used in the test simulations; solid lines for model (1) and dashed lines for model (2).	23
Figure 6.	Test simulation: Simulated hysteretic path for the matrix gridblock at 0.116 m distance from the fracture (a) with model (1) and (b) with model (2).	24
Figure 7.	Test simulation: Simulated liquid saturation and capillary pressure distributions during the fifth year.	25
Figure 8.	Discretized fracture-matrix system used in the studies.	28
Figure 9.	Main drying curve, curve (1), and predicted main wetting curves; from experimental analysis (Kool and Parker, 1987), curve (3), and from Mualem (1977) theoretical models I, curve (4), and II, curve (2).	32
Figure 10.	Main wetting and drying curves and the first-order scanning curves used for model (1) and (2); dotted lines for model (1) and dashed lines for model (2).	34
Figure 11a.	Model (1): Simulated hysteretic paths for gridblock at 0.5 mm from the fracture, 0.25 m depth.	37
Figure 11b.	Model (1): Simulated hysteretic paths for gridblock, center of the matrix, 0.25 m depth.	38
Figure 11c.	Model (1): Simulated hysteretic paths for gridblock at 0.5 mm from the fracture, 1.9 m depth.	39
Figure 11d.	Model (1): Simulated hysteretic paths for gridblock, center of the matrix, 1.9 m depth.	40
Figure 12.	Model (1): Simulated liquid saturations in the fracture.	41
Figure 13a.	Model (1): Simulated liquid saturations for the matrix cross-sections at 0.5 mm distance from the fracture.	43
Figure 13b.	Model (1): Simulated liquid saturations for the matrix cross-section in the center of the matrix.	44

Figure 14.	Model (1): Simulated liquid saturation in the matrix at 0.25 m depth.	45
Figure 15a.	Model (2): Simulated hysteretic paths for gridblock, 0.5 mm from the fracture, 0.25 m depth.	47
Figure 15b.	Model (2): Simulated hysteretic paths for gridblock, center of the matrix, 0.25 m depth.	48
Figure 15c.	Model (2): Simulated hysteretic paths for gridblock, 0.5 mm from the fracture, 1.9 m depth.	49
Figure 15d.	Model (2): Simulated hysteretic paths for gridblock, center of the matrix, 1.9 m depth.	50
Figure 16.	Model (2) versus model (1): Simulated liquid saturations in the fracture.	51
Figure 17.	Model (2) versus model (1): Simulated liquid saturations for the matrix cross-sections at 0.5 mm distance from the fracture.	52
Figure 18.	Model (2) (1 mm volumetric aperture for the fracture): Simulated hysteretic path for the grid block at 0.5 mm from fracture and .75 m depth.	54
Figure 19a.	Model (3): Simulated hysteretic paths for gridblock, 0.5 mm from the fracture, 0.25 m depth.	56
Figure 19b.	Model (3): Simulated hysteretic paths for gridblock, center of the matrix, 0.25 m depth.	57
Figure 19c.	Model (3): Simulated hysteretic paths for gridblock, 0.5 mm from the fracture, 1.9 m depth.	58
Figure 19d.	Model (3): Simulated hysteretic paths for gridblock, center of the matrix, 1.9 m depth.	59
Figure 20.	Model (3): Simulated liquid saturations in the fracture.	60
Figure 21a.	Model (3): Simulated liquid saturations for the matrix cross-section at 0.5 mm distance from the fracture.	61
Figure 21b.	Model (3): Simulated liquid saturations for the matrix cross-section in the center of the matrix.	62
Figure 22.	Model (3): Simulated liquid saturations for the matrix at 0.25 m depth.	63
Figure 23a.	One year wetting/drying cycle: Simulated liquid saturations for the matrix cross section at 0.5 mm distance from the fracture.	65
Figure 23b.	One year wetting/drying cycle: Simulated liquid saturations for the matrix cross section in the center of the matrix.	66
Figure 24a.	One year wetting/drying cycle: Simulated hysteretic path at 0.5 mm distance from the fracture and 0.75 m depth with model (1).	67
Figure 24b.	One year wetting/drying cycle: Simulated hysteretic path at 0.5 mm distance from the fracture and 0.75 m depth with model (2).	68

List of Tables

		Page
Table 1.	Parameters used in the test problem.	21
Table 2.	Parameter values used in the simulations.	29

Abstract

As part of the code development and modeling work being carried out to characterize the flow in the unsaturated zone at Yucca Mountain, Nevada, capillary hysteresis models simulating the history-dependence of the characteristic curves have been developed. The objective of the work has been both to develop the hysteresis models, as well as to obtain some preliminary estimates of the possible hysteresis effects in the fractured rocks at Yucca Mountain given the limitations of presently available data.

Altogether three different models were developed based on work of other investigators reported in the literature. In these three models different principles are used for determining the scanning paths: in model (1) the scanning paths are interpolated from tabulated first-order scanning curves, in model (2) simple interpolation functions are used for scaling the scanning paths from the expressions of the main wetting and main drying curves and in model (3) the scanning paths are determined from expressions derived based on the dependent domain theory of hysteresis.

These models were interfaced with a numerical simulator for unsaturated flow (TOUGH (Transport of Unsaturated Groundwater and Heat) Pruess, 1986) and preliminary simulations were carried out. A system consisting of discrete fractures and rock matrix parts was simulated under periodically occurring infiltration pulses. Comparisons were made between the process taking place along the main drying curve alone and the hysteretic cases. Material properties used represent values reported for the densely welded tuffs at Yucca Mountain, Nevada. The necessary data were derived based on information available in the soils literature because no actual hysteresis measurements are available for the welded tuffs. The results showed a strongly hysteretic behavior near the land surface. This together with the overall weaker matrix capillary suctions generated higher fracture flows in the hysteretic case. Both the fractures and the matrix were affected to greater depths. In the non-hysteretic case the wetting front was sharper but

the influence was not felt as deep as in the hysteretic case. Using the theoretically derived hysteresis model (3) and assuming a heavy rainfall every ten years, after 20 years the pulse had penetrated about 1 m deeper in the hysteretic case than in the non-hysteretic case and the largest local difference in matrix liquid saturation was approximately four percent.

Based on the results presented in this report some recommendations for the future use of the three hysteresis models can also be given. When hysteretic processes with reversals only up to first-order scanning are to be carried out, use of model (1) is recommended because of the ease with which any data can be incorporated into this model. Due to the fact that this type of model is poor in predicting second and higher order scanning curves and can thus yield erroneous results for systems with multiple reversals, we do not recommend the use of model (1) for such cases. If multiple reversals are to be modeled and measured scanning curve data are available, use of model (2) is recommended since this model can be calibrated to fit measured data. Finally, if estimates of hysteresis effects need to be obtained without measured scanning curve data, use of model (3) is probably most justified, because the derivation of this model is based on the theory of hysteresis and should consequently be soil-independent.

Acknowledgments

The authors wish to express their thanks to J. Wang and K. Pruess from Lawrence Berkeley Laboratory, P. Montazer formerly at U.S. Geological Survey and R. Lenhard from Virginia Polytechnic Institute and State University for their helpful discussions, and Y. Tsang and J. Wang from Lawrence Berkeley Laboratory for reviewing this work. This work was carried out under U.S. Department of Energy Contract No. DE-AC03-76SF00098 via the DOE-Nevada Office in cooperation with U.S. Geological Survey in Denver.

1.0. INTRODUCTION

The unsaturated zone at Yucca Mountain, Nevada is being considered as a potential site for storage of nuclear waste. Both field work and theoretical studies are being conducted to characterize the fracture and rock matrix properties at the site and to understand the fluid flow within the system. At present, work is being carried out to develop tools to design and analyze several large-scale field tests planned for the near future.

As part of this work we have developed three capillary hysteresis models that simulate the history dependence of the characteristic curves. The objective of our work has been two fold: (1) to develop hysteresis models for the systems encountered at Yucca Mountain, and to interface the models with unsaturated fluid flow simulators, and (2) to obtain preliminary estimates of the possible hysteresis effects in the fractured rocks at Yucca Mountain within the limitations of presently available data.

In our work we started with a conceptually simple hysteresis model (Niemi and Bodvarsson, 1987; Niemi et al. 1987) and proceeded to more sophisticated ones. Altogether, three different models were developed based on models reported in the literature. The models were incorporated into the numerical simulator TOUGH (Transport of Unsaturated Groundwater and Heat) (Pruess, 1986) and their performance was tested in realistic simulations.

The models, as well as the results of the simulations conducted are presented in this report. Based on the results obtained, recommendations for the future use of the three models is given.

2.0. BACKGROUND ON HYSTERESIS

Capillary pressure (ψ) - liquid saturation (S) relation for unsaturated flow is usually described by a single-valued function of the form $\psi = \psi(S)$, in which each liquid saturation value corresponds to only one capillary pressure value. Hysteresis causes this relation to become history-dependent and one liquid saturation can correspond to any of the capillary pressures falling within the hysteresis envelope defined by the so-called main wetting and main drying curves. Which one of these values is the correct one for a given situation, depends on the previous wetting/drying history of the system, or, more specifically, on the hysteretic path along which the system has previously been wetting and/or drying.

A hypothetical example of hysteretic data consisting of the main wetting and main drying curves is shown in Figure 1 (solid lines). A main drying curve is a curve along which the process takes place if the system is continuously drying from a fully saturated state. A main wetting curve is a curve along which the process takes place in case of continuous wetting from the residual saturation. If the system, while drying along the main drying curve, begins to rewet, the process starts to follow a so-called first-order (wetting) scanning curve. Similarly, reversals from the main wetting curve are followed by scanning along first-order (drying) scanning curves. Subsequent reversals from first-order curves are followed by scanning along second-order curves, reversals from the second-order curves by scanning along third-order curves and so on. Examples of hysteretic paths with multiple reversals are also shown in Figure 1.

A hysteretic path generated by, for example, a first-order and a second-order curve or by a second-order and a third-order curve always tends to close forming a looplike path. In other words, a second-order curve converges towards the point were the first-order curve diverted from the main boundary curve; similarly a third-order curve con-

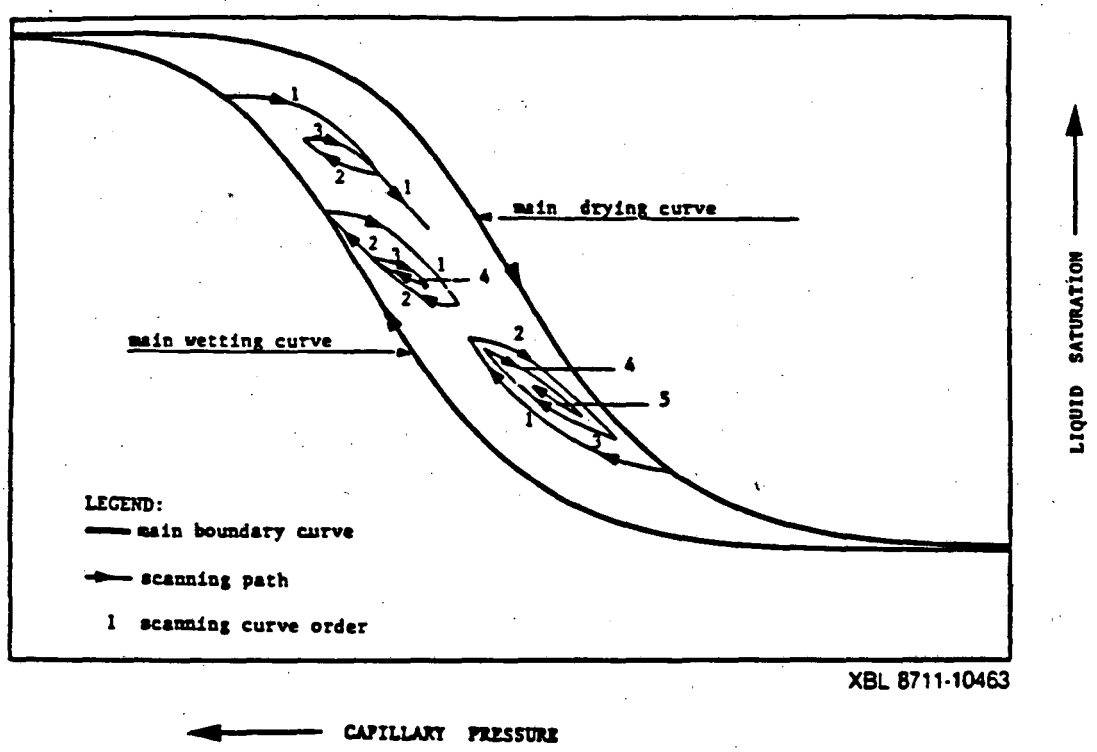

Figure 1. Examples of hypothetical hysteretic paths.

verges towards the point where the second-order curve diverted from the first-order curve and so on (e.g. Banerjee and Watson, 1984 and Parker and Lenhard, 1988). The "closing" property of hysteresis loops is not enforced in many of the hysteresis models that have been published. The error that can be generated, when the closing is not demanded is known in the hysteresis literature as the "pumping effect," (Klute and Heermann, 1974 and Jaynes, 1984). An example of this kind of erroneous result is shown in Figure 2.

2.1. Measurements

Hysteresis in unsaturated porous medium has previously been studied using materials with relatively weak capillary pressures such as sand, class beads, clay and loams (Poulovassilis and Childs, 1971; Klute and Heermann, 1974; Mualem, 1974; Cary, 1975; Dane and Wierenga, 1975; Lees and Watson, 1975; Mualem and Dagan, 1975; Poulovassilis and Tzimas, 1975; Perrens and Watson, 1977; Banerjee and Watson, 1984 and Curtis and Watson, 1984). All of these materials have significantly weaker capillary pressures than the welded tuffs encountered at Yucca Mountain, for which capillary pressures of tens of bars have been measured.

Daily et al. (1987) conducted wetting/drying experiments with a fractured tuff sample at different temperatures and attributed the irreversibility of the dehydration /rehydration processes to hysteresis. However, quantitative estimates of the possible hysteresis effects in the fracture or in the matrix have not been derived.

The presence of hysteresis in the capillary pressure-water content ($\psi = \psi(\theta)$) relation, or equivalently, in the capillary pressure-liquid saturation ($\psi = \psi(S)$) relation, as well as in the relative permeability-capillary pressure ($k_{rl} = k_{rl}(\psi)$) relation is well established for many materials. There is, however, disagreement about whether there is significant hysteresis in the relative permeability-liquid saturation relation. After reviewing related measurements Pickens and Gillham (1980) concluded that the majority of published data seems to indicate that the relation $k_{rl} = k_{rl}(S)$ can be assumed to be non-hysteretic for all

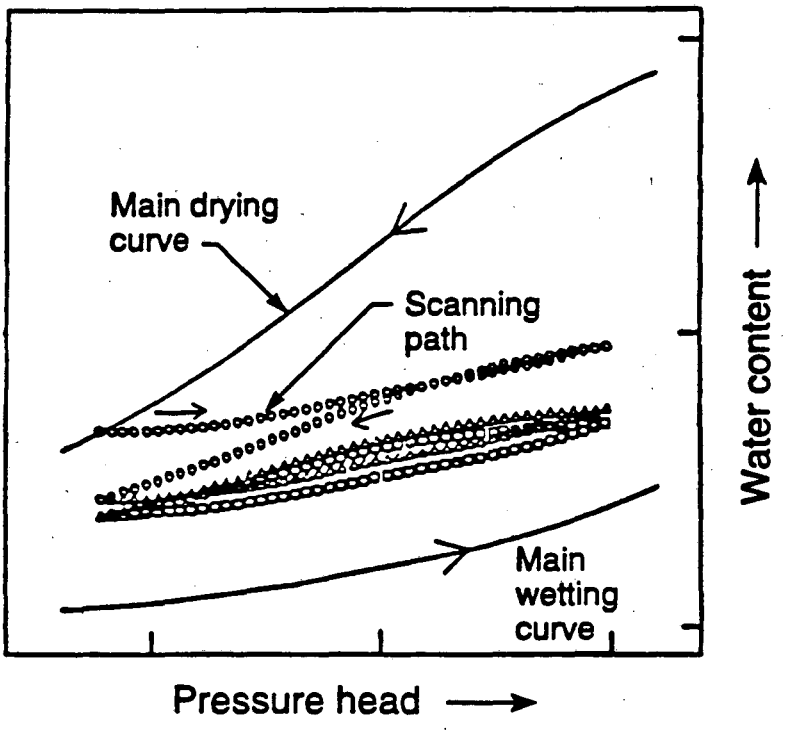

Figure 2. Example of the "pumping effect" (Klute and Heermann, 1974 and Jaynes, 1984).

practical purposes.

Related measurements or discussions are presented by Topp and Miller (1966), Topp (1969), Topp (1971), Vachaud and Thony (1971), Poulovassilis and Tzimas (1975), Gillham et al. (1976), Mualem (1976), Aggelides and Youngs (1978), Pickens and Gillham (1980), and Kool and Parker (1987).

2.2. Models

The capillary hysteresis models reported in the literature can be categorized into three groups:

(1) Interpolative models.

(2) Models employing empirical closed-formed expressions.

(3) Models based on the domain theory of hysteresis.

In the interpolative models, the main boundary and the first-order scanning curves are given in tabulated form. All values inside the main envelope (region defined by the main wetting and main drying curves) are determined from the tabulated first-order curves through interpolation. In doing so it is assumed that second- and higher-order scanning curves can be approximated from the first-order curves. This method has been used by Whisler and Watson (1969), Watson and Perrens (1973), Curtis (1977), Perrens and Watson (1977) and Curtis and Watson (1984).

Dane and Wierenga (1975), Killough (1976), Hoa et al. (1977), Pickens and Gillham (1980), Scott et al. (1983), and Kool and Parker (1987) have used closed-form expressions to calculate the scanning curves. Most of these models are developed for a specific soil and do not claim general validity, although in some cases their predictions are tested with different soils.

The domain models are based on theoretical representation of capillary hysteresis. According to the domain theory, the total volume of pores in the soil can be divided into subvolumes (domains) each of which has a characteristic wetting and drying pore radii

(or is characterized by a pair of capillary pressure intervals $\Delta\phi$ and $\Delta\phi w$ at which the domain drains and rewets). The distribution of these domains, expressed in terms of distribution functions, determines the hysteretic behavior of the soil. Domain models can be divided into two groups: Models treating the pores as independent of the neighboring pores are called independent domain models and models which attempt to take into account the influence of the neighboring pores are called dependent domain models. Domain models have been developed by Poulovassilis (1962) Poulovassilis and Childs (1971), Topp (1971), Mualem (1974), Mualem and Dagan (1975), Lees and Watson (1975), Poulovassilis and Tzimas (1975), Mualem (1976), Banerjee and Watson (1984), and Mualem (1984), among others.

In comparison with the other methods, the most sophisticated dependent domain models are probably the most accurate in predicting scanning curves for different media (see, for example, Kool and Parker, 1987). However, the accuracy of these models (for example, models of Mualem and Dagan (1975) and Banerjee and Watson (1984)) is achieved by using considerable amounts of data for calibration (data of first-order scanning curves is also needed). The formulation as well as computational aspects of these models are also more complicated. The modified dependent domain model of Mualem (1984) requires only the main wetting and drying curves for calibration. However, only expressions for the first- and second-order scanning curves are given in this work.

3.0. DEVELOPMENT OF HYSTERESIS MODELS USED

For our work we developed modeling capabilities for three different models describing the hysteretic capillary pressure-liquid saturation relation. Based on the literature cited, the relative permeability-liquid saturation relation was assumed non-hysteretic for each model. In the numerical algorithms capillary pressure is computed as a function of liquid saturation from the appropriate scanning curve, or, in special cases, the appropriate boundary curve. The equation of the appropriate curve for a given timestep is determined for each numerical element based on the previous wetting/drying history. Given the type of path element followed during the previous timesteps, along with information as to whether the liquid saturation is increasing or decreasing, the program determines the type of path at the current timestep. If the same curve is used as in the previous timestep, the exact location of the path is known and the capillary pressure can be determined. If a reversal from the previous curve is taking place, the equation of the new path must be determined first. This is done by assuming that the point of reversal is located at the solution point at the end of the previous timestep.

3.1. Interpolation from First-Order Scanning Curves (model (1))

In the first hysteresis model, (model (1)) the interpolation method is used. Tabulated data on boundary curves and first-order scanning curves are input and used for interpolation. When a reversal from the previous wetting or drying curve occurs, the program finds the interval in which the turning point falls and solves the equation of the new scanning curve through interpolation between the tabulated curves of correct type below and above the turning point. A complete description of this model and instructions for incorporation into a numerical flow simulator are given in Niemi and Bodvarsson (1987) and Niemi et al. (1987).

The interpolation method was chosen for its conceptual simplicity and the fact that any kind of experimental data can be easily incorporated into the model.

The major weakness of the interpolation method is that the closing of the hysteretic loops is not enforced. With frequent reversals from wetting to drying and vice versa, approximation of the higher-order scanning curves through the first-order scanning curves can produce an erroneous "pumping effect" (Figure 2). If the wetting and drying periods are short, the higher-order scanning curves do not necessarily produce loop-like paths such as those shown in Figure 1. This phenomenon, which has been demonstrated by Klute and Heermann (1974) and Jaynes (1984) is not limited to interpolation models, but can occur with all the models for which closing of the hysteresis loops is not required. According to Banerjee and Watson (1984), this type of method should not be used when frequent reversals from wetting to drying or vice versa are modeled. Perrens and Watson (1977) also refer to this limitation, but conclude that the approach generally describes most redistribution events with sufficient accuracy.

3.2. Empirical Model Using Interpolation Functions (Model (2))

The second model, which was based on the work of Killough (1976), uses simple interpolation functions for determining the scanning paths as functions of the capillary pressures on the main wetting and drying curves. Expressions for the main wetting and main drying curves need to be known.

The equations of the scanning paths are chosen such that the hysteretic path always tends to close at the original point of reversal on the limiting boundary curve. This prevents pumping effects. The first-order scanning curves are assumed to converge towards the maximum attainable saturation in the case of wetting scanning, or towards the residual saturation in the case of drying scanning. After a reversal from these curves, the equations for the second-order scanning curves are determined by assuming that the curves converge towards the original point of reversal on the main boundary curve.

The capillary pressures on a wetting scanning curve are determined from

$$\psi(S) = \psi_d(S) - F \cdot \left[\psi_d(S) - \psi_w(S)\right] \tag{1a}$$

where

ψ_d = capillary pressure on the main drying curve
ψ_w = capillary pressure on the main wetting curve
S = liquid saturation

and

$$F = \frac{\dfrac{1}{S - S_{dep} + \varepsilon} - \dfrac{1}{\varepsilon}}{\dfrac{1}{S_{as} - S_{dep} + \varepsilon} - \dfrac{1}{\varepsilon}} \tag{1b}$$

where

S_{dep} = departure point saturation
S_{as} = asymptotic saturation
ε = curvature coefficient

Equations (1a) and (1b) (Killough, 1976) are valid for both first- and second-order wetting scanning curves. In the case of first-order wetting scanning (curve 2 in Figure 3), the departure saturation is the actual reversal point saturation SDEP1 and the asymptotic saturation is equal to the maximum attainable saturation SMAX (Figure 3). In the case of second-order wetting-scanning (curve 4 in Figure 3), departure saturation is equal to the saturation at an imaginary reversal point (point SDEP* in Figure 3). The location of the imaginary point is determined based on the assumption that the wetting-scanning and drying-scanning curves (curves 4 and 3, respectively in Figure 3) must intersect at the turning point (point A). The asymptotic saturation for a second-order scanning curve is the saturation of the original point of reversal (point SDEP2 in Figure 3).

For drying-scanning the capillary pressures are determined from:

$$\psi(S) = \psi_w(S) + FF \cdot \left[\psi_d(S) - \psi_w(S)\right] \tag{2a}$$

where

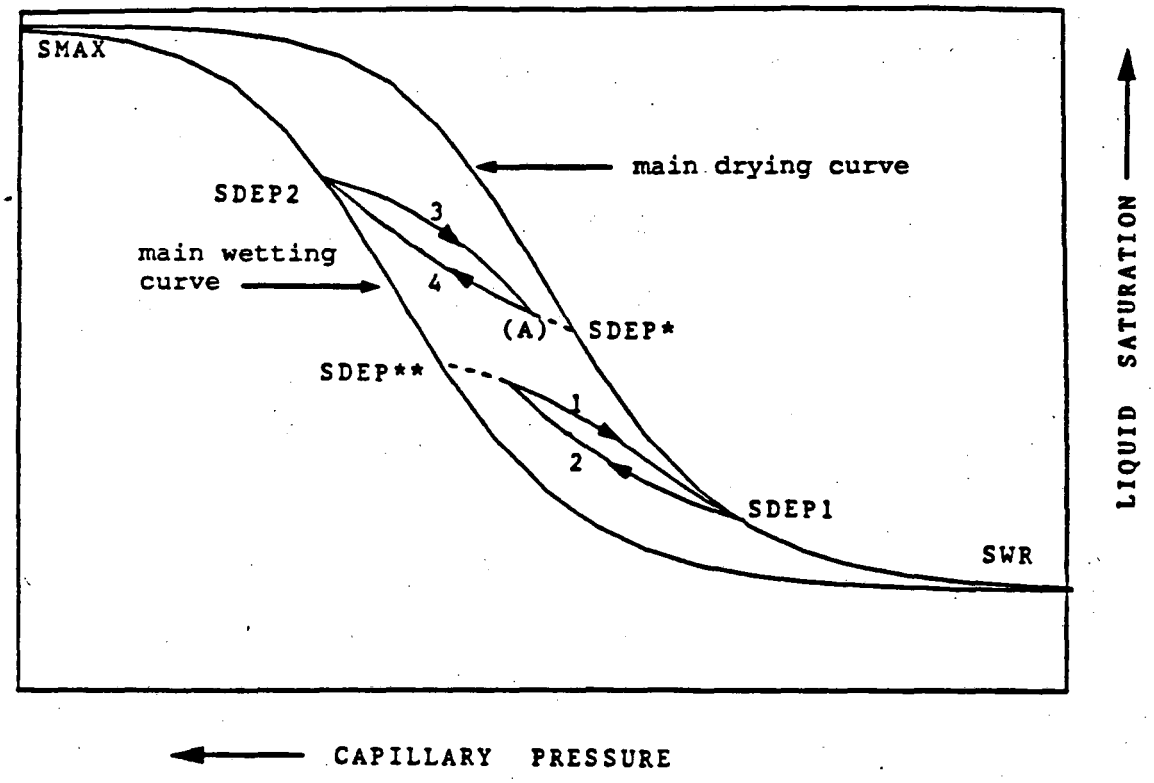

Figure 3. Example of scanning paths generated with model (2).

$$FF = \frac{\dfrac{1}{S_{dep} - S + \varepsilon} - \dfrac{1}{\varepsilon}}{\dfrac{1}{S_{dep} - S_{as} + \varepsilon} - \dfrac{1}{\varepsilon}} \tag{2b}$$

For first-order drying scanning curves (curve 3 in Figure 3) the departure saturation is again the actual departure point saturation (SDEP2 in Figure 3) and the asymptotic saturation is the residual saturation (SWR in Figure 3). For second-order scanning (curve (1) in Figure 3) the values to be used are the imaginary reversal saturation (SDEP** in Figure 3) and the saturation at the original point of reversal on the main drying curve (SDEP1 in Figure 3).

Examination of Equations 1b and 2b shows that increasing the value of ε decreases the curvature of the scanning curve. For example in the case of Equation 1b F is inversely proportional to liquid saturation S, thus yielding stronger curvatures near the point of reversal. With the value $\varepsilon = 0$ the dependence is strongest and increasing the value of ε weakens this inverse dependence thus yielding scanning curves with less curvature.

The model can be adjusted to fit measured scanning curve data by varying the curvature coefficient ε. Killough (1976) developed the model for three-phase petroleum reservoirs and reported values of ε in the range of 0.05 to 0.1 for his data. Since the model is empirical in nature it should be calibrated using some measured scanning curve data.

Capillary pressures on the main wetting and drying curves, which are used in Equations (1) and (2), can be computed for example by using closed-form van Genuchten expressions:

$$\psi = \frac{1}{\alpha}\left[\left(\frac{S_{max} - S_{min}}{S - S_{min}}\right)^{1/m} - 1\right]^{1/n} \tag{3}$$

where

S_{max} = maximum liquid saturation
S_{min} = residual liquid saturation
α,m,n = van Genuchten parameters

The higher-order scanning curves are treated in the model in a simple manner suggested by Killough (1976); if a reversal from second-order to third-order scanning takes place, the scanning returns to the original first-order scanning curve and no separate expression is used for the third-order curves. Consequently the following fourth-order curves are computed as second-order curves converging towards the point of reversal on the main boundary curve. This is a simplifying assumption, since the true third-order scanning path would rather lie between the first- and second-order curves and converge towards the intersection point of these curves and the true fourth-order curve would lie between the third- and second-order curve converging towards the intersection of these two curves (see Figure 1). This assumption, however, preserves the simplicity of the model without generating significant errors. The inaccuracies generated are of much smaller magnitude than the "pumping" effects discussed earlier. If separate expressions were given for the third- and fourth-order curves, Equations (1) and (2) could be used by choosing the reversal and asymptotic values appropriately and by using the first- and second-order curves for "scaling" instead of the main boundary curves used above. By doing so, however, the amount of "history" information to be stored as well as the computational effort needed for obtaining a value on a higher order curve becomes prohibitively large. The gained increase in accuracy does not necessarily justify this increase in complexity. The simplifying assumption used will be discussed further later in this report, when the results of some simulations are examined.

3.3. Model Using the Dependent Domain Theory (Model (3))

The third model was modified from the dependent domain model of Mualem (1984). Unlike the two previous models the domain models are derived based on theoretical presentation of hysteresis and should therefore be independent of soil type. Also,

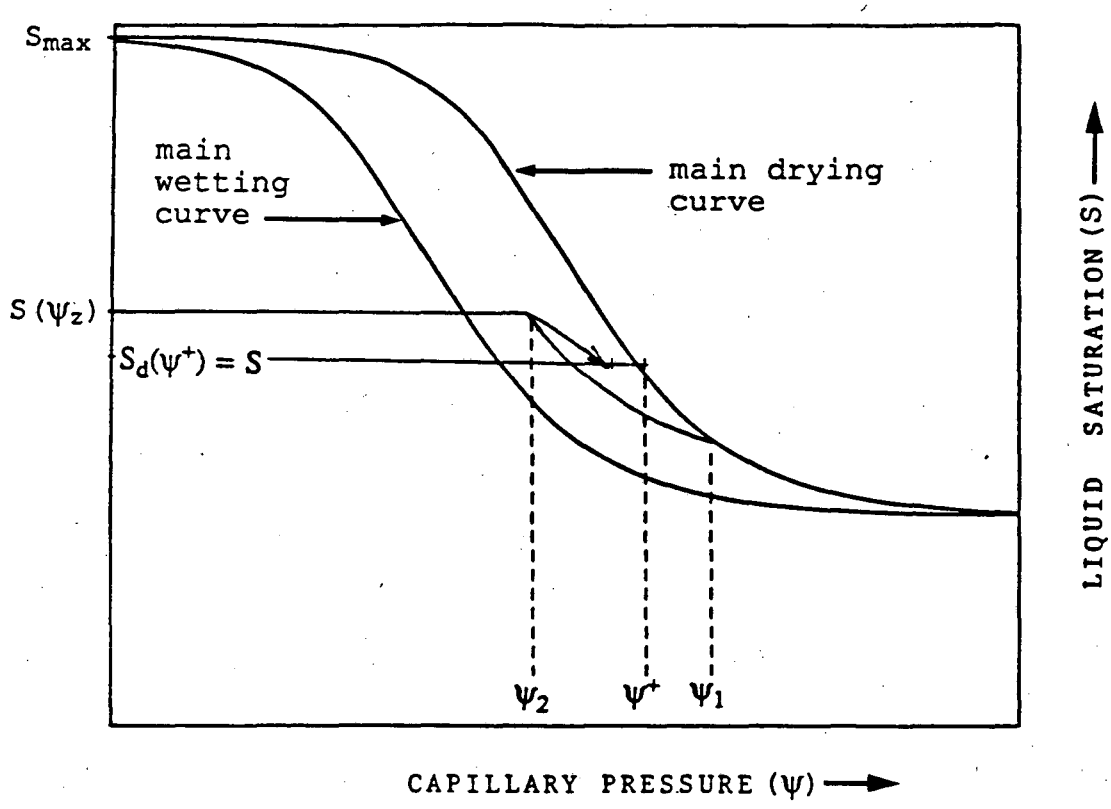

Figure 4. Parameters for scanning paths with model (3).

based on results of comparison studies between model predictions and experimental measurements, the dependent domain models have probably proven to be the most accurate of the available hysteresis models in predicting scanning curves for different media (see, for example, Kool and Parker, 1987).

Also for this model the expressions of the main-wetting and drying curves need to be known. We compute these as continuous van Genuchten expressions of the form of Equation (3). The expressions for the scanning curves are computed internally based on the dependent domain theory. Unlike in the case of model (2) no calibration factor is used in the expressions.

For the first-order wetting scanning curve the following relation is used:

$$S = S_d(\psi_1) + \frac{[S_{max} - S_d(\psi_1)]}{[S_{max} - S_w(\psi_1)]^2} [S_{max} - S_w(\psi_1)] [S_w(\psi) - S_w(\psi_1)] \tag{4}$$

where

S = liquid saturation on the scanning curve
S_d = liquid saturation on the main drying curve
S_w = liquid saturation on the main wetting curve
ψ_1 = capillary pressure at the point of reversal from the main drying curve to the first-order wetting scanning.

In the numerical flow simulator used in our studies (TOUGH; Pruess, 1986) liquid saturation is solved as one of the three "primary" variables and capillary pressures are solved as "secondary" variables as a function of S. Because of this, we use Equation (4) for solving for $S_w(\psi)$, which is the only unknown in the expression, if S is known. Maximum liquid saturation S_{max} is an input parameter, reversal capillary pressure ψ_1 is saved when the reversal takes place, and $S_d(\psi_1)$ and $S_w(\psi_1)$ can be solved from the expressions for the main drying and wetting curves. Once $S_w(\psi)$ is solved the corresponding ψ can be solved from the equation of the main wetting curve. The parameters in Equation (4) are shown in Figure 4.

For the second-order drying scanning curve the expression is

$$S = S(\psi_2) - \frac{[S_{max} - S_d(\psi^+)]}{[S_{max} - S_w(\psi^+)]^2} [S_{max} - S_w(\psi)] [S_w(\psi_2) - S_w(\psi)] \tag{5}$$

where

$S(\psi_2)$= liquid saturation at the point of reversal from first-order wetting scanning to second-order drying scanning

ψ_2 = capillary pressure at point of reversal from first-order wetting scanning to second-order drying scanning

ψ^+ = capillary pressure for which $S_d(\psi^+) = S$.

Again, the only unknown in Equation (5) is $S_w(\psi)$. Reversal values $S(\psi_2)$ and ψ_2 are saved when the reversal takes place; thus, $S_w(\psi_2)$ can also be determined. Capillary pressure ψ^+ can be solved from the expression for the main drying curve as a function of S. $S_w(\psi)$ can then be solved from Equation (5), with the resulting parabolic equation yielding two solutions for $S_w(\psi)$. With the aid of simple algebra it can be shown that only one of the solutions is smaller than $S_w(\psi_2)$ and the equation thus yields only one meaningful value for $S_w(\psi)$. Once $S_w(\psi)$ is known, capillary pressure can again be solved from the expression of the main wetting curve (Figure 4).

Mualem (1984) only gives expressions for the first- and second-order scanning curves. For our simulations additional expressions are needed for higher-order scanning curves. As discussed earlier, the basic concepts of hysteresis require the higher-order scanning curves to have shapes that allow the hysteresis loops at each level to close. If, for example, the system begins to rewet, while drying along a second-order drying curve, the wetting will take place along a third-order wetting curve that converges towards the reversal point from first-order wetting to second-order drying. If this reversal point is reached and the system continues to wet, the process follows the original first-order wetting scanning curve and "forgets" the previous higher-order curves. If, instead, the system begins to dry before reaching this convergence point, the process follows a fourth-order drying scanning curve that converges towards the reversal point from second-order drying to third-order wetting. As the order of the scanning curve gets higher, the width of the envelope becomes narrower and refining the process beyond the third-order curves

is probably not meaningful (Parker and Lenhard, 1988).

In order to maintain the simplicity of our model without significant loss of accuracy, we approximated the third- and higher-order scanning curves as log-straight lines between the latest reversal point and the correct point of convergence. This simplification was considered reasonable in the light of the results of Jaynes (1984). He compared four different hysteresis models and concluded that the entire process from first-order scanning curves on, could be presented with straight lines with reasonable accuracy (linear hysteresis model), and recommended the use of this type of model over more complicated ones due to its simplicity.

4.0. TEST SIMULATIONS WITH MODELS (1) AND (2)

As a first step, simulations were carried out to test the performance of hysteresis models (1) and (2) with realistic material properties. For this purpose a very simplified fracture-matrix system was modeled.

4.1. System Modeled

The system modeled is shown in Figure 5a. A matrix "slice" discretized with a MINC-type (Multiple Interacting Continua) mesh (Pruess, 1983) is assumed to be surrounded by fractures on all four sides. Our interest is to examine the matrix response under alternating wetting/drying conditions; the fractures are treated as variable boundary conditions for the matrix. During the wetting periods the fractures are assigned a constant "high" liquid saturation representing a rainy period; during the drying period they are assigned a constant "low" saturation representing a dry period. Assuming that during pulse infiltration conditions all incoming flow will go initially into the fractures, and assuming that the flow in the fractures is due to gravity alone, a first-order estimate for fracture liquid saturation near the land surface for given fracture properties and given flux can be obtained through Darcy's law. The value of liquid saturation computed in this manner was used as the wetting period fracture liquid saturation. During the drying periods, fracture liquid saturations are assumed to be $\approx 0\,(1 \times 10^{-5})$. It should be noted that by doing so we assume instantaneous changes (from wetting to drying and vice versa) in the fracture saturations. We also ignore the amount of water lost from fractures into the matrix. However, since the objective of these first simulations is to test the model performance rather than to obtain reliable estimates of hysteresis effects, errors generated by these assumptions are not relevant.

The material properties used are summarized in Table 1. The hysteresis data for

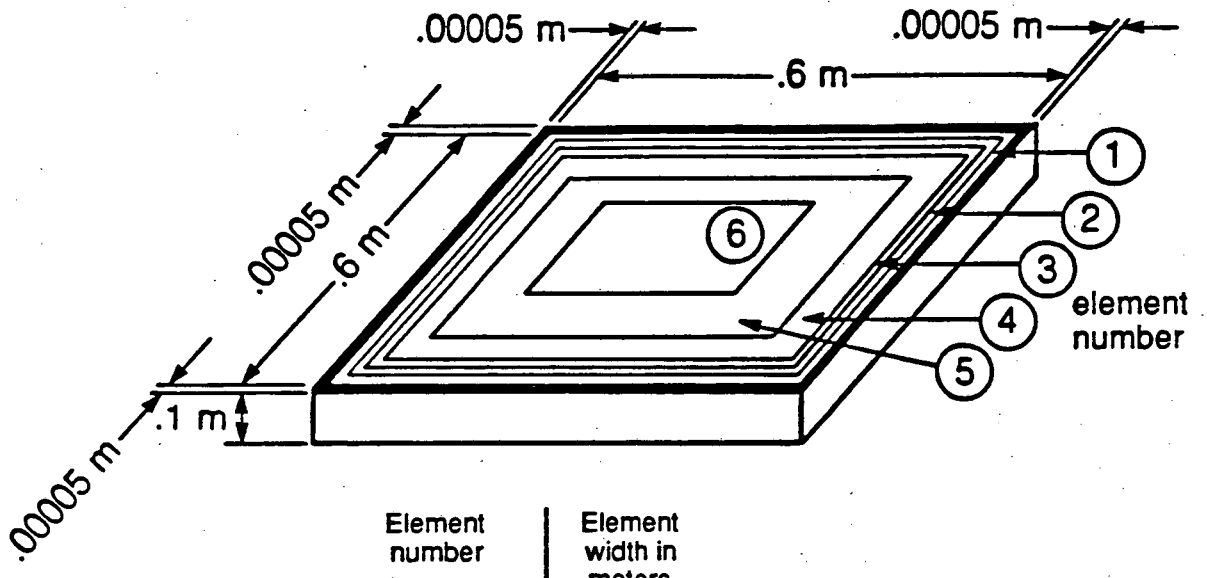

Element number	Element width in meters
1	0.001
2	0.005
3	0.01
4	0.05
5	0.1
6	0.268

XBL 8612-12789

Figure 5a. Discretized flow region used in the test simulations.

Table 1. Parameters used in the test problem[1]

Parameter	Fracture[2]	Matrix
Absolute Permeability -horizontal -vertical	 2.0×10^{-12} 2.0×10^{-10}	 2.4×10^{-18} 2.4×10^{-18}
Relative Permeability	$k_{rl} = S_l^{1.936}$	$k_{rl} = 10^{4.619(S_l-1)}$ (for $S_l > 0.507$)
Capillary Pressure (1) Non-hysteretic (2) hysteretic; Model #1 (3) hysteretic; Model #2	 $\psi = 0.0134\ S_l^{0.491}$ (bars) $\psi = 0.0134\ S_l^{0.491}$ (bars) $\psi = 0.0134\ S_l^{0.491}$ (bars)	 Tabulated main wetting curve in Figure 5. Hysteresis data in Figure 5. Main wetting and drying curves [5] in Figure 5; $\varepsilon = 0.05$
Porosity	1.00	0.12
Aperture[3]	0.1 mm	
Liquid Saturation	0.0049 during wetting[4] 1×10^{-5} during drying	uniform initial liquid saturation of 0.71

Notes:

1. Source Rulon et al. (1986).
2. Fracture parameters are only used for determining the wetting period fracture liquid saturation.
3. Corresponds to an air entry value of 0.0134 bars if determined from the capillary rise equation

$$\rho_{aev} = \frac{2\gamma}{\delta}$$

   where γ, interfacial tension of water, $= 0.07\ kg/s^2$, δ = aperture (m)
4. Corresponds to ≈ 0.2 mm/yr infiltration concentrated into a three-month period, assuming that all water goes into fractures and is transported by gravity forces alone.
5. Continuous van Genucten (1980) expressions (Equation 3) with;
   for main drying: $S_{max} = 0.984$, $S_{min} = 0.318$, $m = 0.671$, $n = 3.040$, $\alpha = 1.147\ bar^{-1}$;
   for main wetting: $S_{max} = 1$, $S_{min} = 0.002$, $m = 0.358$, $n = 1.558$, $\alpha = 8.4 \times 10^{-2}\ bar^{-1}$

this set of simulations were generated by using the matrix characteristic curve for the welded units reported by Rulon et al. (1986) as the main wetting curve. The curves for these units reported by Klavetter and Peters (1986) are used as the basis for the main drying curve. The resulting data are shown in Figure 5b.

4.2. Simulations and Results

Three sets of simulations were carried out. In the first set, non-hysteretic matrix capillary pressure-liquid saturation relation was assumed. The non-hysteretic process followed the curve specified as the main wetting curve in Figure 5b. For the second set of simulations model (1) was used, and in the third set model (2) was used. Wetting periods corresponding to an infiltration of 0.2 mm/yr concentrated into three-month wetting periods were assumed to last for three months, after which a nine-month drying period followed. The cycle was repeated five times.

The simulated hysteretic scanning paths for one matrix element obtained with models (1) and (2) are shown in Figures 6a and 6b, respectively. The corresponding non-hysteretic process took place along the main wetting curve. As can be seen from the figure, model (1) produces a "pumping" effect between the first and second cycles. This is a result of both the structure of the model and the coarseness with which the main wetting curve is tabulated in the region of question (the main wetting curve is approximated as log-straight lines between tabulated values rather than as a continuous line as in model (2)). After the first cycle the predictions of the two hysteretic models are very similar.

The simulated matrix liquid saturation and capillary pressure distributions during the fifth year are shown in Figure 7. As can be seen, the non-hysteretic case and the two hysteretic cases differ significantly while the predictions of the two hysteretic cases are very similar (their differences are not resolved in Figure 7 except for the liquid saturations at the end of the drying period).

The big difference between the non-hysteretic and the two hysteretic cases can be

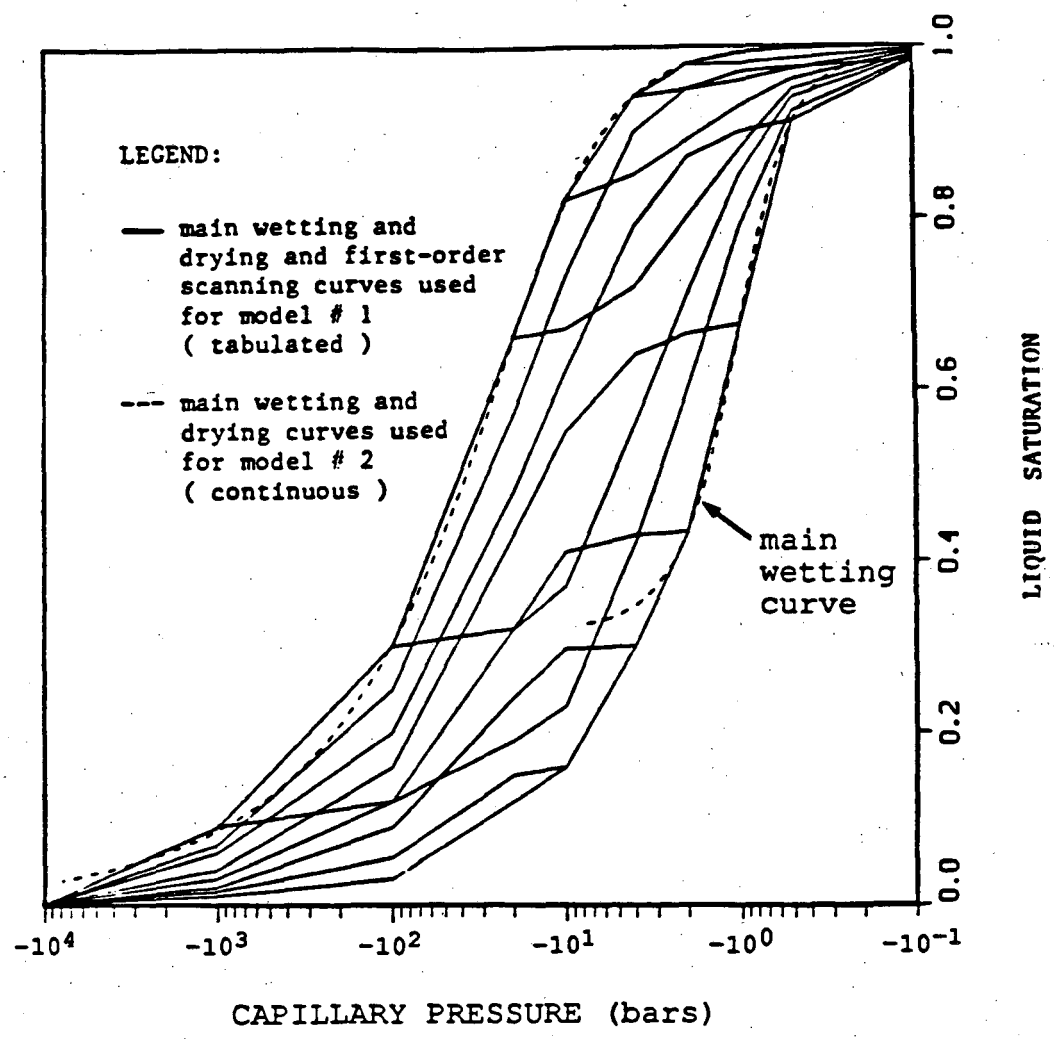

Figure 5b. Hypothetical hysteresis data used in the test simulations; solid lines for model (1) and dashed lines for model (2).

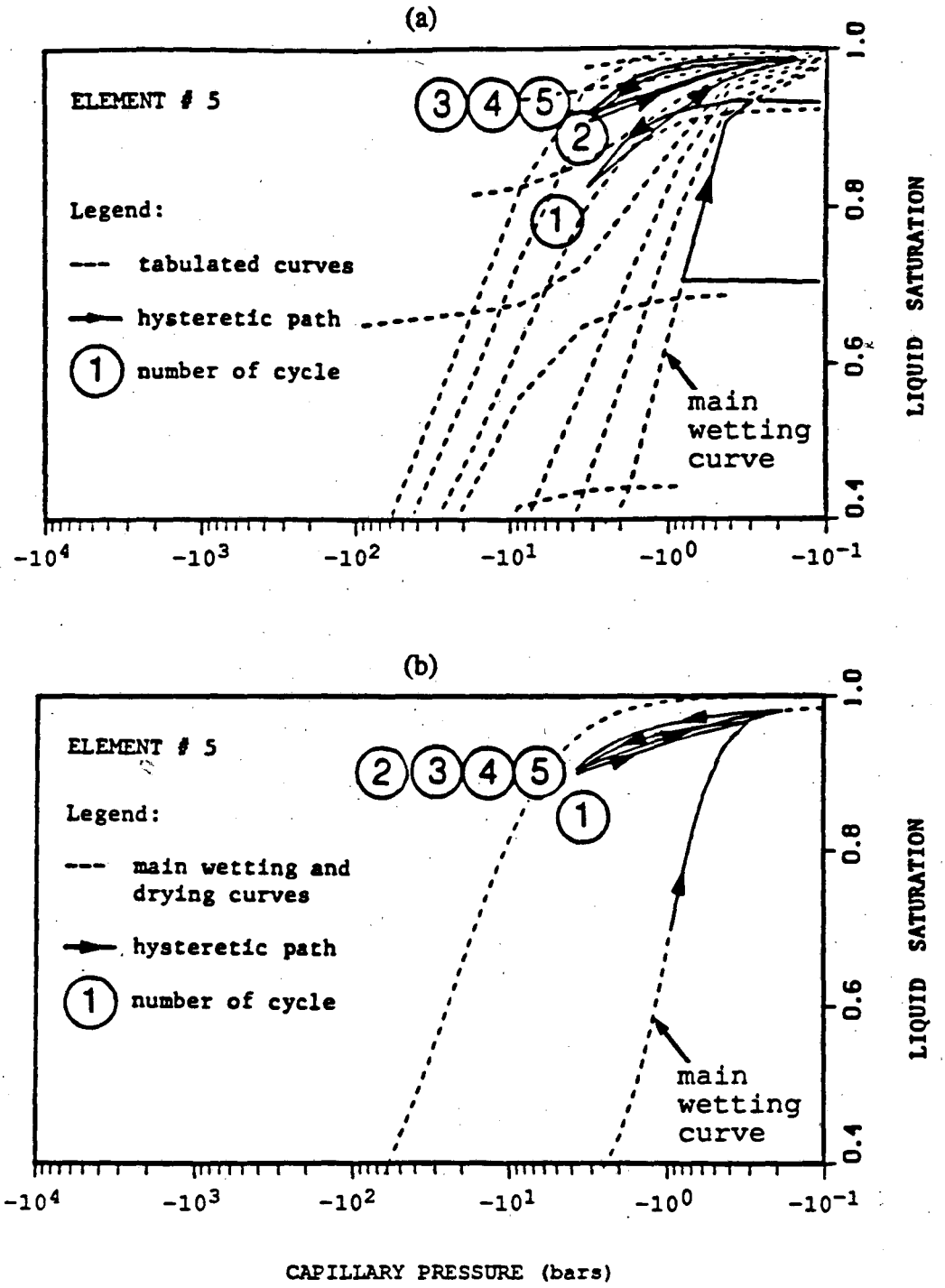

Figure 6. Test simulation: Simulated hysteretic path for the matrix gridblock at 0.116 m distance from the fracture (a) with model (1) and (b) with model (2).

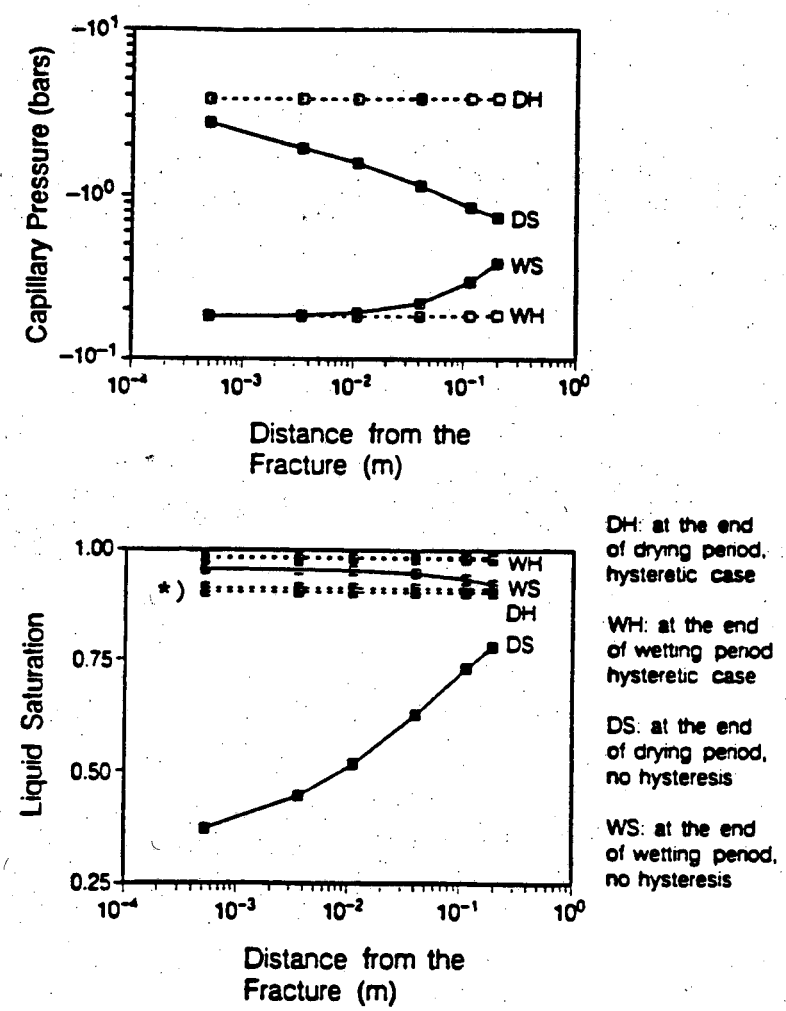

*) lower dashed line with model 2.

Figure 7. Test simulation: Simulated liquid saturation and capillary pressure distributions during the fifth year.

easily explained through Figures 6a and 6b. In the hysteretic cases the system is shifted into considerably higher liquid saturation range than in the non-hysteretic case, where the process occurs along the main wetting curve. The higher liquid saturations correspond to higher relative permeabilities and more mobile fluid. Consequently, the matrix response to variations in the fracture is faster and equilibrium with the fracture is reached faster in the hysteretic cases. The overall values in liquid saturation are also very different (Figure 7). However, it should be emphasized that because of the highly hypothetical nature of the hysteresis data used, no quantitative estimates of the possible hysteresis effects should be made based on these results. As will be discussed later in this report, data from soils literature indicate that the ratio of the α–parameters in the van Genuchten expression between the main drying and wetting curves is generally on the order of $\alpha_{wetting}/\alpha_{drying} \approx 2$. For the data in Figure 5b this ratio is ≈ 13, which corresponds to a very wide hysteresis envelope. In the simulations presented later in this report, with which we actually wanted to obtain estimates of possible hysteresis effects, ratios of ≈ 2 were used.

5.0. CAPILLARY HYSTERESIS SIMULATIONS FOR FRACTURED ROCK UNDER VARIABLE INFILTRATION CONDITIONS

In the simulations presented here we examine infiltration pulse penetration in an idealized fractured rock system. The system was chosen to represent conditions similar to those thought to be present in the welded units at Yucca Mountain within the limitations of available data at the present time.

Pulse penetration within the unsaturated zone at Yucca Mountain has been previously studied by Wang and Narasimhan (1986). Their study was carried out without considering hysteresis effects.

In our work we studied the system both with and without hysteresis. Hysteresis effects are likely to be more pronounced in matrix flow than in fracture flow (Montazer and Wilson, 1984). Therefore, in our studies hysteresis was only considered for the matrix flow; flow in the fractures was assumed non-hysteretic. All three hysteresis models were used and their results were compared with each other and with the non-hysteresis case.

5.1. System Modeled

The fracture-matrix model used was idealized as consisting of discrete vertical fractures and matrix columns. According to Wang and Narasimhan (1985), the presence of horizontal fractures does not significantly affect the vertical fluid flow for conditions similar to those used in this study. Therefore, the horizontal fractures were not included in our model and a system consisting of a matrix column bounded by four orthogonal vertical fractures was modeled. In the horizontal plane the the matrix was discretized using a MINC-type mesh (Pruess, 1983) with element width increasing with distance from the fracture. The mesh used is shown in Figure 8.

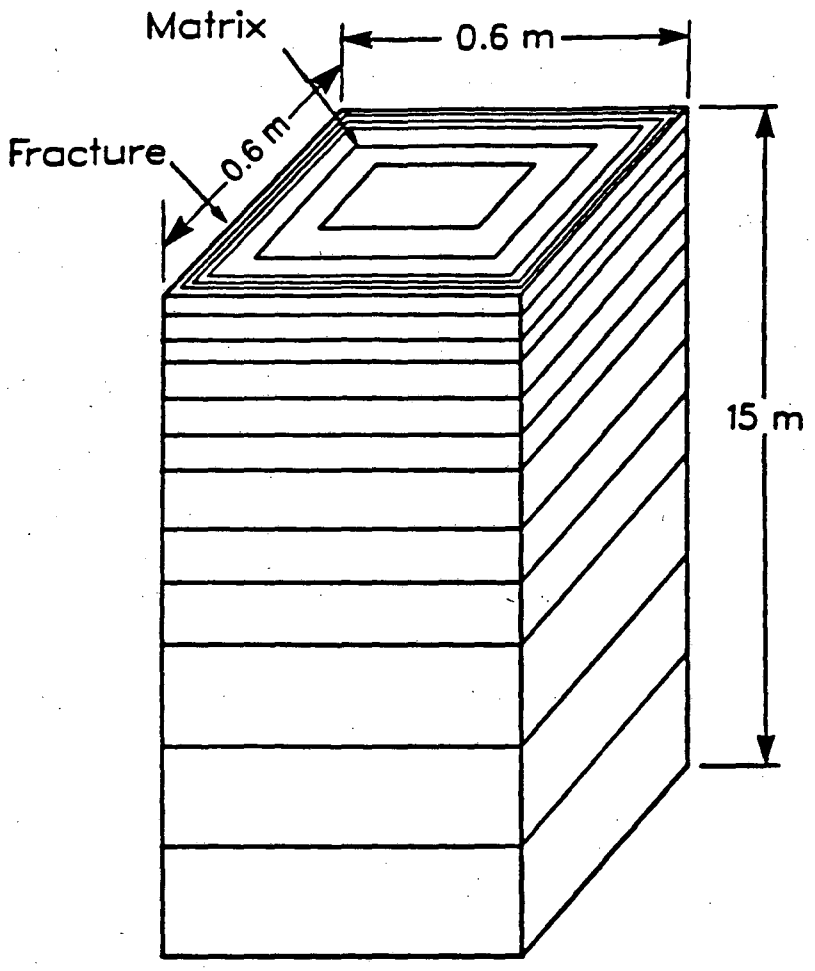

horizontal discretization (m):

0.0001 (fracture),0.001,0.005,0.01,0.05,0.1,0.268

vertical discretization (m):

3 x 0.5, 3 x 0.833, 3 x 1.333, 3 x 2.333

Figure 8. Discretized fracture-matrix system used in the studies.

Table 2. Parameter values used in the simulations.

Matrix	
• porosity	$\phi_m = .12$
• absolute permeability	$k_m = 3.9 \cdot 10^{-18}\ m^2$
• capillary pressure	-[2]non-hysteretic; Curve (1) in Figure 9. -[3]hysteretic, Models #1 and #2; data shown in Figure 10. -[2]hysteretic Model #3; main drying and main wetting curves Curves (1) and (3) in Figure 9.
• relative permeability[2]	$k_{rl} = \left[\frac{S-S_{min}}{S_{max}-S_{min}}\right]^{1/2}\left\{1-\left[1-\left(\frac{S-S_{min}}{S_{max}-S_{min}}\right)^{1/m}\right]^{m}\right\}^{2}$
Initial Conditions	
• capillary pressures	$\psi_m = -.968$ bars
• liquid saturation	$S_l = .691$
Fracture	
• aperture[4]	$\delta_f = .1$mm
• porosity	$\phi_f = 1.$
• spacing	$D = .60$m
• absolute permeability per fracture[5]	$k_f = 8.33 \cdot 10^{-10}\ m^2$
• relative permeability	$k_{rl} = S_l^{1.936}$
• capillary pressure	$\psi_f = .0134 \cdot S_l^{-.491}$ bars
Initial Conditions	
• capillary pressure[6]	$\psi = -.968$ bars
• liquid saturation	$S_l = .164 \cdot 10^{-3}$

Notes:

1. Source Rulon et al. (1986), unless otherwise indicated.
2. van Genuchten parameters (Eq. 3): $S_{max} = 0.984$, $S_{min} = 0.318$, $m = 0.671$, $n = 3.040$, $\alpha_{drying} = \alpha_{nonhyst} = 1.147$ 1/bar (all after Rulon et al. (1986) and $\alpha_{wetting} = 2.294$ 1/bar (see Section 5.2).
3. van Genuchten parameters (Eq. 3): for main drying curve as in (2) and for main wetting curve $S_{max} = .89$, $S_{min} = .2$, $m = .6$, $n = 2.5$, $\alpha = 2.5$ 1/bar (see Section 5.2 for explanation).
4. Fracture aperture approximately corresponds to the air entry value = 0.0134 bar through the capillary rise equation (see Table 1).
5. Permeability determined from cubic law; $k_f = (\delta_f)^2/12$.
6. Assuming capillary pressure equilibrium between the fracture and the matrix.

The material properties used are summarized in Table 2. They correspond to values reported for the welded units at Yucca Mountain by Rulon et al. (1986), with the exception of the hysteresis data for the matrix, which is discussed in a later section. The fracture properties were obtained by using a parallel plate model (see, for example, Witherspoon et al., 1980) along with the theoretically derived fracture characteristic curves reported for the welded units by Rulon et al. (1986).

For the matrix, an initial liquid saturation of 0.69 was used. The initial liquid saturation for the fractures was obtained by assuming capillary pressure equilibrium between the fractures and the matrix. With these initial conditions and the material properties shown in Table 2, steady state flow through the matrix is about 0.1 mm/yr and the flow through the fracture is about 5% of the matrix flow rate. For the lower boundary a constant pressure boundary condition was specified, which allowed for a liquid outflow corresponding to the background liquid flux. The mesh was sufficiently large that the pulse effects did not reach this boundary. Using symmetry considerations, no-flow boundary conditions were specified at the sides of the system (assuming uniform fracture spacing). For the upper boundary a varying flux boundary condition was used to represent the periodically varying infiltration.

An intense rain period was assumed to take place every 10 years. For each 10-year cycle a pulse infiltration corresponding to 1 mm/yr precipitation for 10 years, concentrated in a 3-month period (1 mm/yr x 10 yr/.25 yr = 40 mm/yr) was introduced for 3 months. During the rest of the cycle (9.75 yrs) only the constant background infiltration rate of 0.1 mm/yr was applied. This cycle was repeated twice. Based on the discussions of Beven and Germann (1982) and Wang and Narasimhan (1985) the macropore (fracture) flow is initiated when the infiltration exceeds the matrix capacity (amount of flow through a fully saturated matrix). In our study the saturated matrix capacity is 1.2 mm/yr; thus, the flow exceeding the background infiltration of 0.1 mm/yr was introduced directly into the fractures.

The problem was first solved by assuming a non-hysteretic $\psi = \psi(S)$ relation. For this case the process was assumed to occur along the curve used as the main drying curve for all the hysteresis simulations. These results were then used, as a base case against which the results from the hysteresis simulations could be compared. One set of simulations was carried out with a smaller pulse and a one-year cycle. Some of the parameter values used in this set of simulations were different from those described above.

5.2. Hysteresis Data

For each of the hysteresis models used the expressions for the main drying and main wetting curves must be known. For model (1) the first-order scanning curves also need to be known. Models (2) and (3) generate these expressions internally. At present, limited moisture-retention data are available for the welded tuffs at Yucca Mountain. These data have been used to simulate water migration through the system (Rulon et al., 1986). Using these data as our main drying curve (curve (1) in Figure 9), the expression for the main wetting curve was predicted by using available information from soil literature.

Based on theoretical models Mualem (1977) has derived two simple formulas (model I and model II) for the prediction of the relationship between the main wetting and main drying curves. When one of the curves is known, the other can be predicted using those expressions. For model I the relation is given by

$$\theta_d(\psi) = 2[\theta_{max} \cdot \theta_w(\psi)]^{1/2} - \theta_w(\psi) \tag{6}$$

and for model II

$$\theta_d(\psi) = [2 \cdot \theta_{max} - \theta_w(\psi)]^{1/2} \cdot \left[\frac{\theta_w(\psi)}{\theta_{max}}\right] \tag{7}$$

where θ is normalized with respect to the residual water content,

θ_d = normalized water content on the main drying curve
θ_w = normalized water content on the main wetting curve
θ_{max} = normalized maximum water content

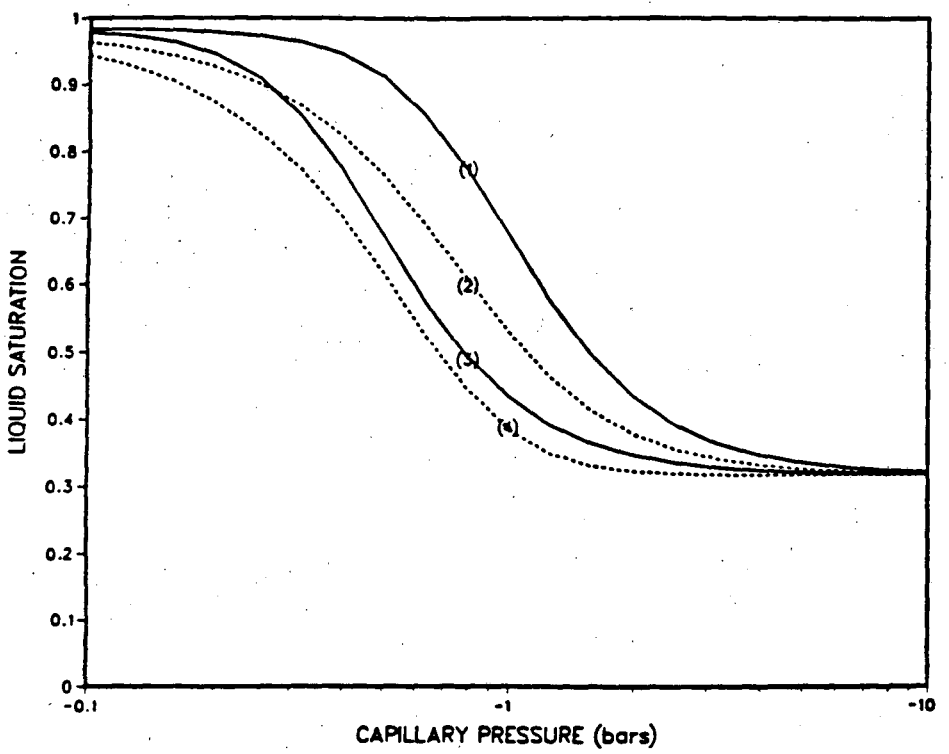

Figure 9. Main drying curve, curve (1), and predicted main wetting curves; from experimental analysis (Kool and Parker, 1987), curve (3), and from Mualem (1977) theoretical models I, curve (4), and II, curve (2).

Using these expressions along with the equation of the main drying curve, we get two predictions for the main wetting curve. These are shown as curve (4) (model I) and curve (2) (model II) in Figure 9.

Expressions (6) and (7) are derived based on independent domain models using the so-called extended similarity hypothesis, and should ideally be valid for all soils. The difference between the two models is the pore domain distribution diagram used in their derivations: the Neél diagram (Mualem, 1977) was used for model (I) and the Mualem diagram for model (II). Mualem (1977) compared the predictions obtained by the two models against experimental data for several soils. The results showed that model (I) failed to reproduce the observed shapes, whereas model (II) gave good results in some of the cases. But for soils where the effect of water blockage against air entry is apparent (high and well defined air entry value), model (II) only yielded good predictions at low saturations, whereas at higher saturations the predictions were poor.

Kool and Parker (1987) analyzed hysteresis measurements for eight different soils by computing the α-parameters of the van Genuchten expression (see Equation 3) for the main wetting and main drying curves. They obtained the mean ratio $\alpha_{wetting}/\alpha_{drying} = 2.08$, with a standard deviation of 0.46. They concluded that the ratio $\alpha_{wetting}/\alpha_{drying} = 2.0$ would provide a useful approximation in cases where data are lacking. The main wetting curve obtained by using this empirical approach is shown in Figure 9 as curve (3). Of the three predicted wetting curves, curve (3) was selected for use with the hysteresis model 3.

For hysteresis models 1 and 2, a slightly different data set was used. These data are shown in Figure 10. In the figure the ratio $\alpha_{wetting}/\alpha_{drying} = 2.2$, which is close to that assumed for model (3) and also well within the range reported by Kool and Parker (1987). The convergence of the main wetting and main drying curve at high saturations is slower in Figure 10 than in Figure 9. In Figure 9 at a capillary pressure of 0.1 bars curve (3) has practically converged with the curve (1), whereas in Figure 10, the ratio of the water contents on the main wetting and main curves is $\theta_{wt}/\theta_{dr} \approx 0.89$. Although in

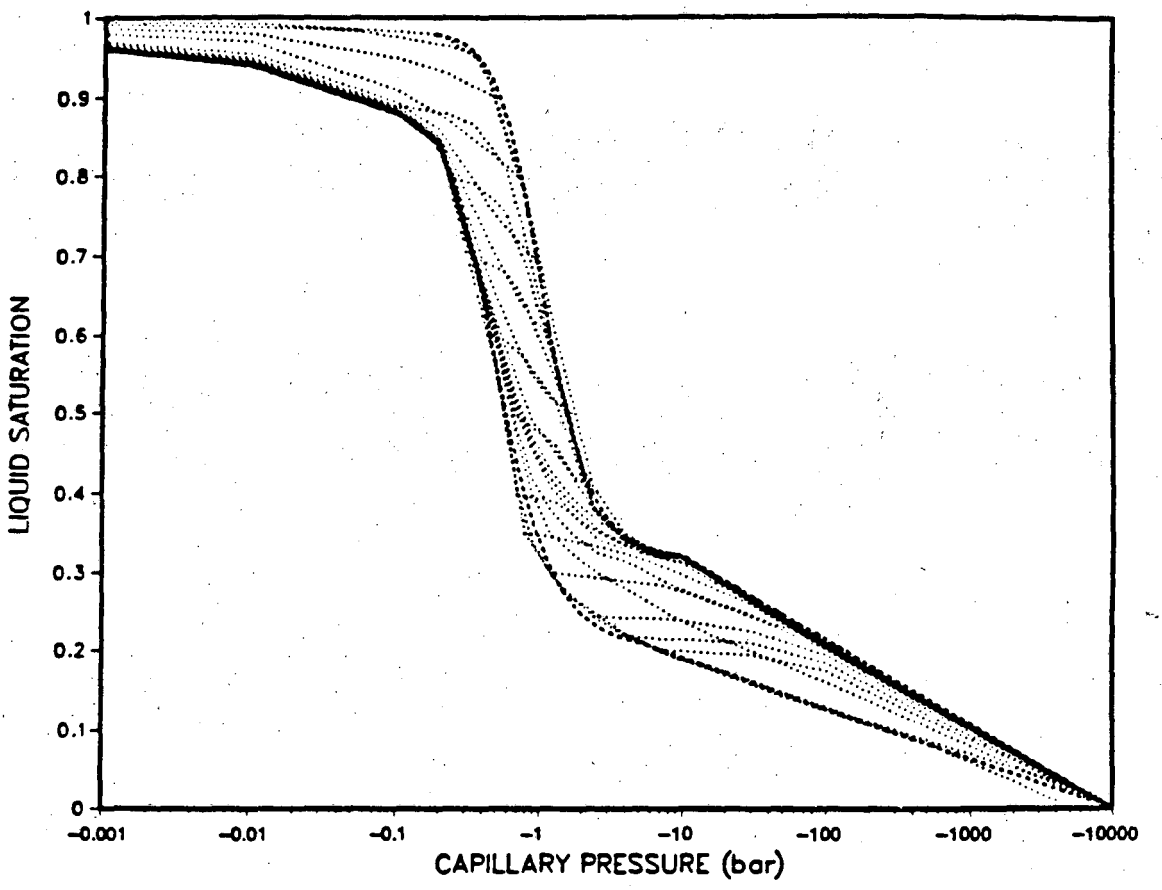

Figure 10. Main wetting and drying curves and the first-order scanning curves used for model (1) and (2); dotted lines for model (1) and dashed lines for model (2).

most hysteresis literature the main boundary curves are assumed to converge towards the same maximum saturation, there is some experimental evidence (e.g., Kool and Parker, 1987) that the maximum saturation on main wetting curve falls below the corresponding value on the main drying curve. Van Genuchten (1980) has reported measured main wetting and drying curves for the Guelph Loam in a capillary pressure range relatively similar to those used in our study (ψ values in his data are about an order of magnitude lower in comparison to the several orders of magnitude difference for most other soils). In his data θ_{wt}/θ_{dr} is about 0.83 at maximum saturation.

The use of different expressions for the main wetting curve makes comparison of the predictions from model (3) with those from models (1) and (2) somewhat difficult. This comparison would in any case not be very meaningful until measured scanning curve data become available for the materials studied. As pointed out earlier the derivation of models (1) and (2) is empirical in nature and experimental data are needed for their calibration, which are not presently available. Model (3), on the other hand, is derived based on the theory of hysteresis, and should therefore be independent of soil type.

We will, however, compare the results obtained with models (1) and (2). For this purpose the first-order scanning curves tabulated for model (1) were generated with the same equations (Equations 1 and 2) that are used internally in model (2) for generating the first-order scanning curves for this model. Thus, the two models should give similar results in the case of first-order scanning and the possible pumping effects of model (1) with higher-order curves can be easily estimated. The resulting scanning curves are shown in Figure 10. For the calibration parameter in Equations (1) and (2) a value of $\varepsilon = 0.05$ was used, which corresponds to the lower limit of the experimental values reported by Killough (1976), and consequently yields most curvature presenting a "worst case" situation.

5.3. Simulations with Model (1) (Ten-Year Cycle)

The problem described earlier was simulated using the hysteresis model (1). In this set of simulations the parameter values given in Table 2 and the hysteresis data shown in Figure 10 were used and the 3 mos/10 yr infiltration cycle described earlier was imposed on the system.

Figure 11a through 11d show the computed hysteretic paths for some of the matrix elements during the two cycles simulated. The hysteretic behavior is strongest in the uppermost layer (Figures 11a and 11b). With increasing depth the oscillations become smaller and in the fourth layer from the top (at the depth 1.9 m) the system is continuously wetting along the first-order wetting curves (Figures 11c and 11d).

If the simulated hysteretic paths in Figures 11a through 11d are examined, it can be seen that no significant pumping takes place in these trace elements. In Figures 11a and 11b we see that the wetting/drying oscillations are large enough for the hysteretic path to become loop-like, with the loops almost closing. The loop is fully closed if the third-order wetting curve, along which the process takes place after reversal from the first drying period, converges towards the point where the system began to dry after the first pulse (3 months in Figure 11a).

The simulated liquid saturations in the fractures at the end of the first pulse (3 months) and at the end of the second recovery (drying) period (20 yrs) are shown in Figure 12 for both the case involving hysteresis and the non-hysteretic case, in which the process takes place along the main drying curve. This figure shows that at the end of the first pulse the liquid saturations in the fractures are considerably higher in the hysteretic case than in the non-hysteretic case. This can be explained by inspecting the results shown in Figures 11a through 11d. When the matrix starts to wet along a first-order wetting curve instead of the main drying curve used in the non-hysteretic case, the capillary suction for a given liquid saturation is smaller and the system gets "shifted" into lower liquid saturation range, which also corresponds to lower relative permeabilities.

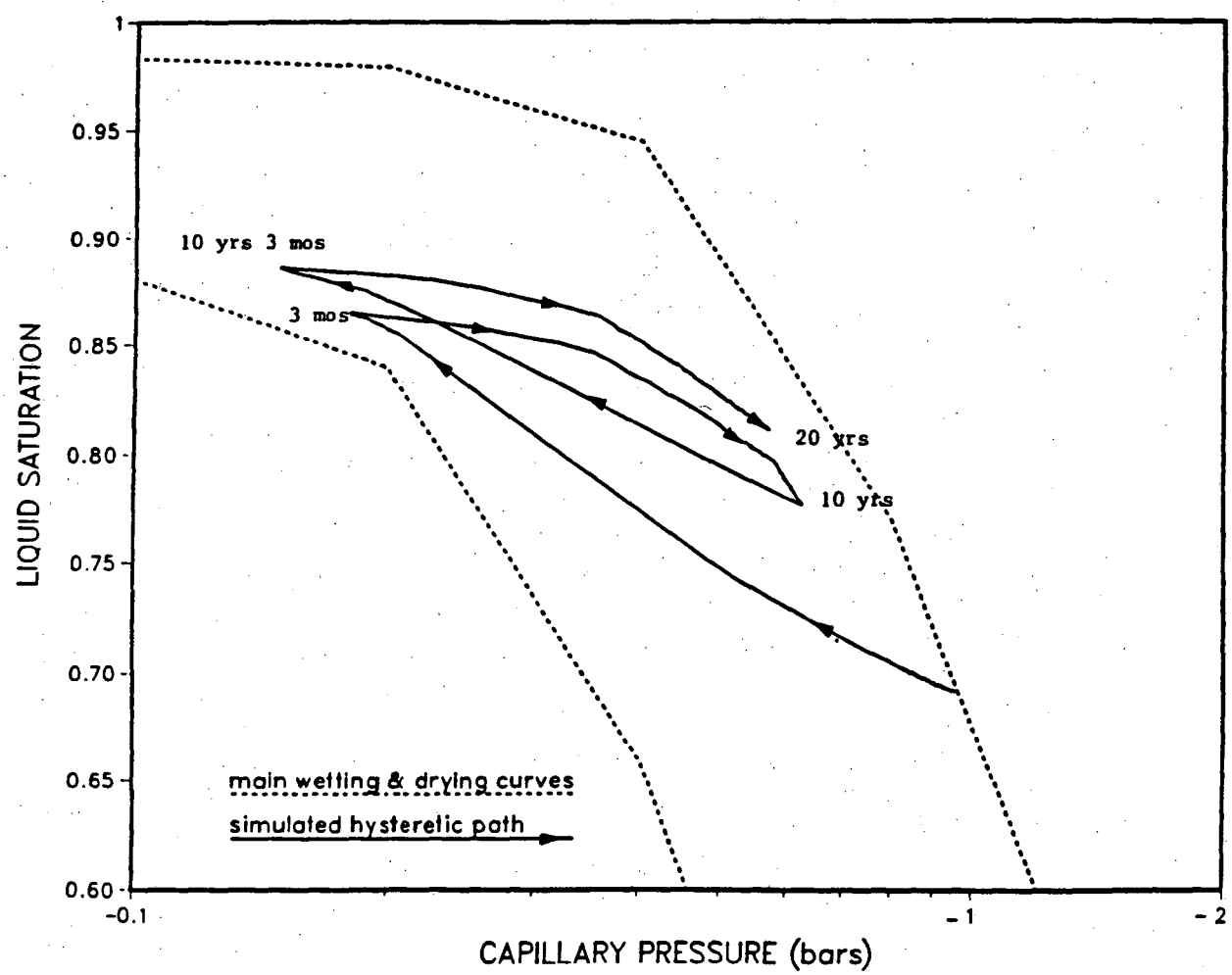

Figure 11a. Model (1): Simulated hysteretic paths for gridblock at 0.5 mm from the fracture, 0.25 m depth.

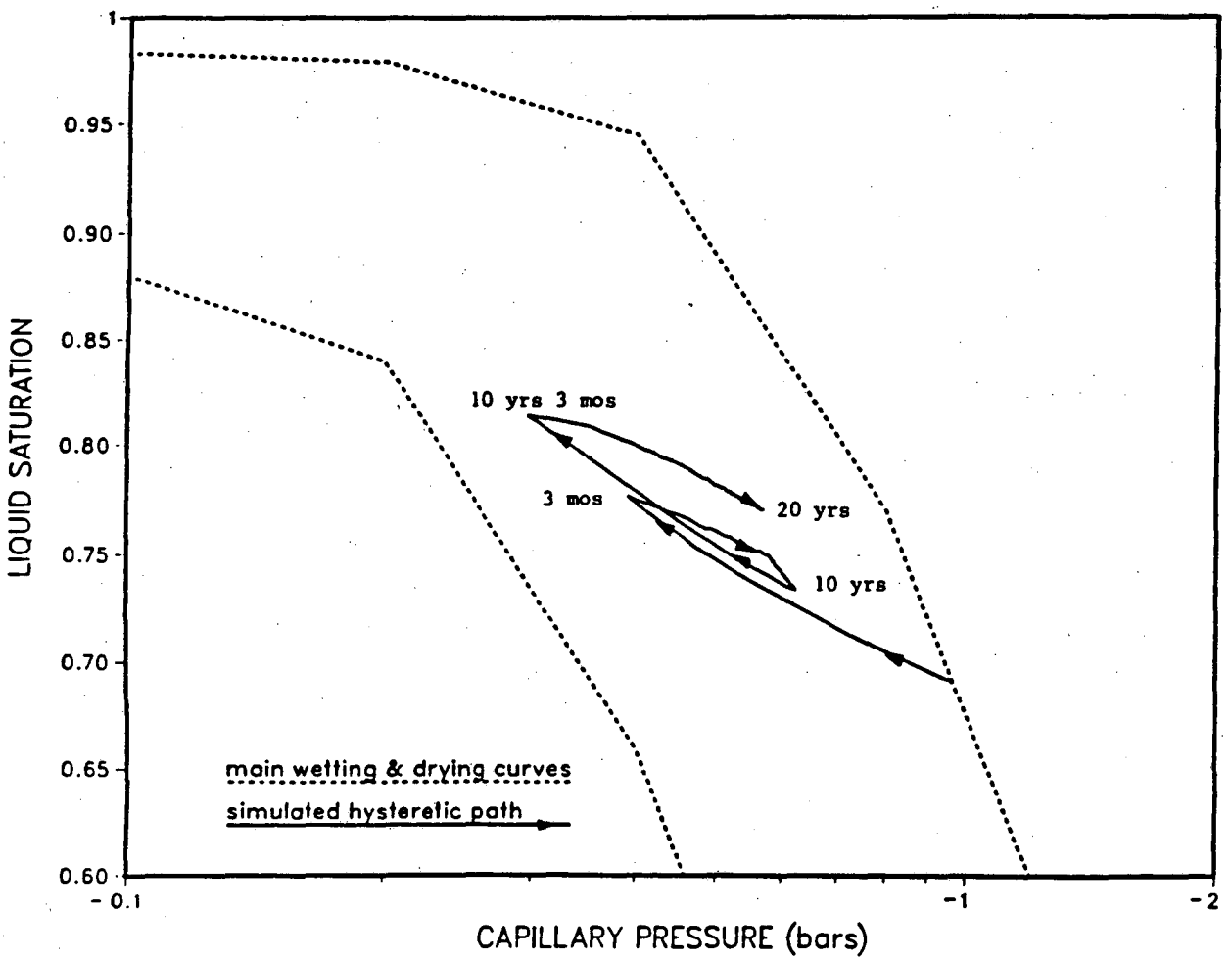

Figure 11b. Model (1): Simulated hysteretic paths for gridblock, center of the matrix, 0.25 m depth.

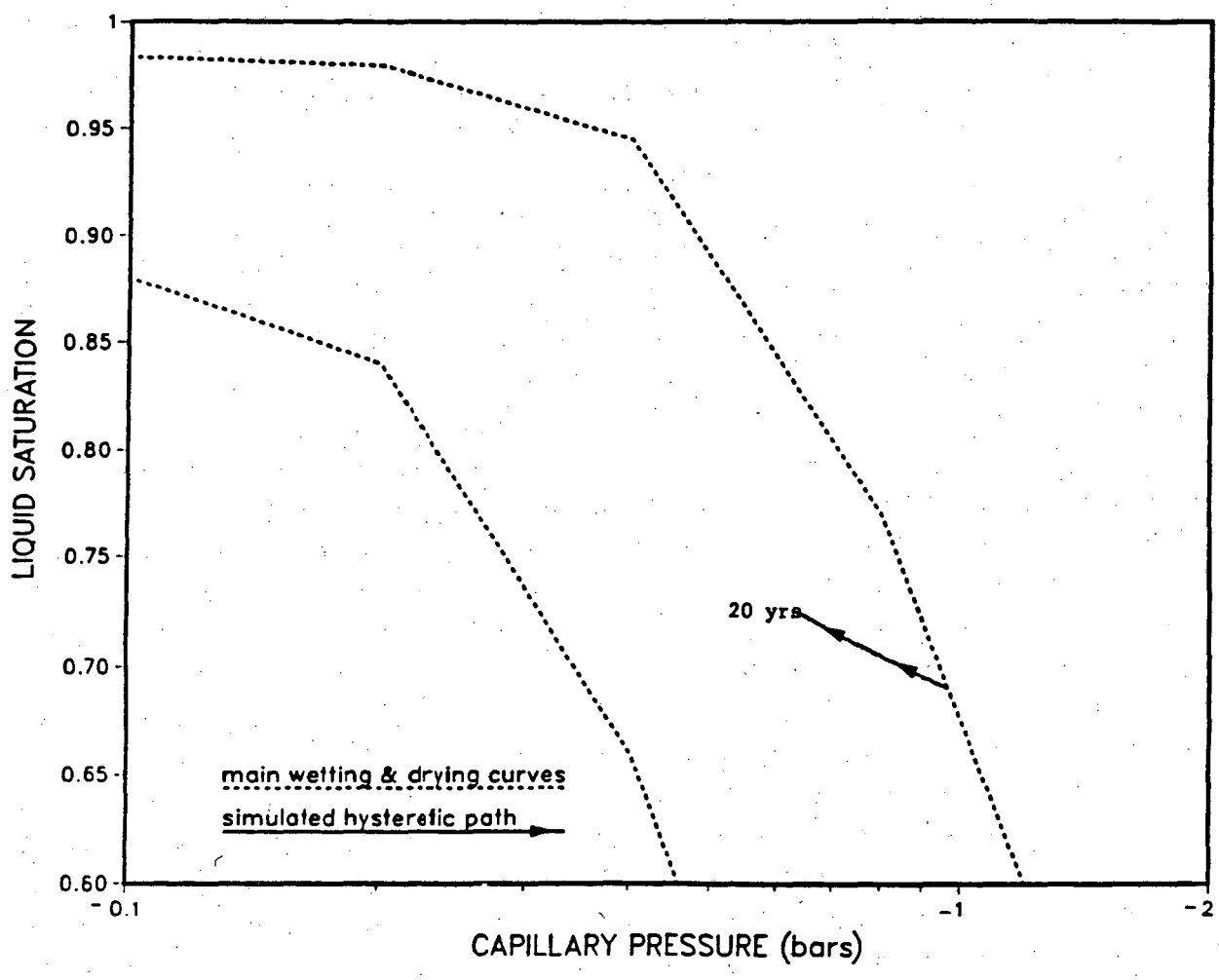

Figure 11c. Model (1): Simulated hysteretic paths for gridblock, at 0.5 mm from the fracture, 1.9 m depth.

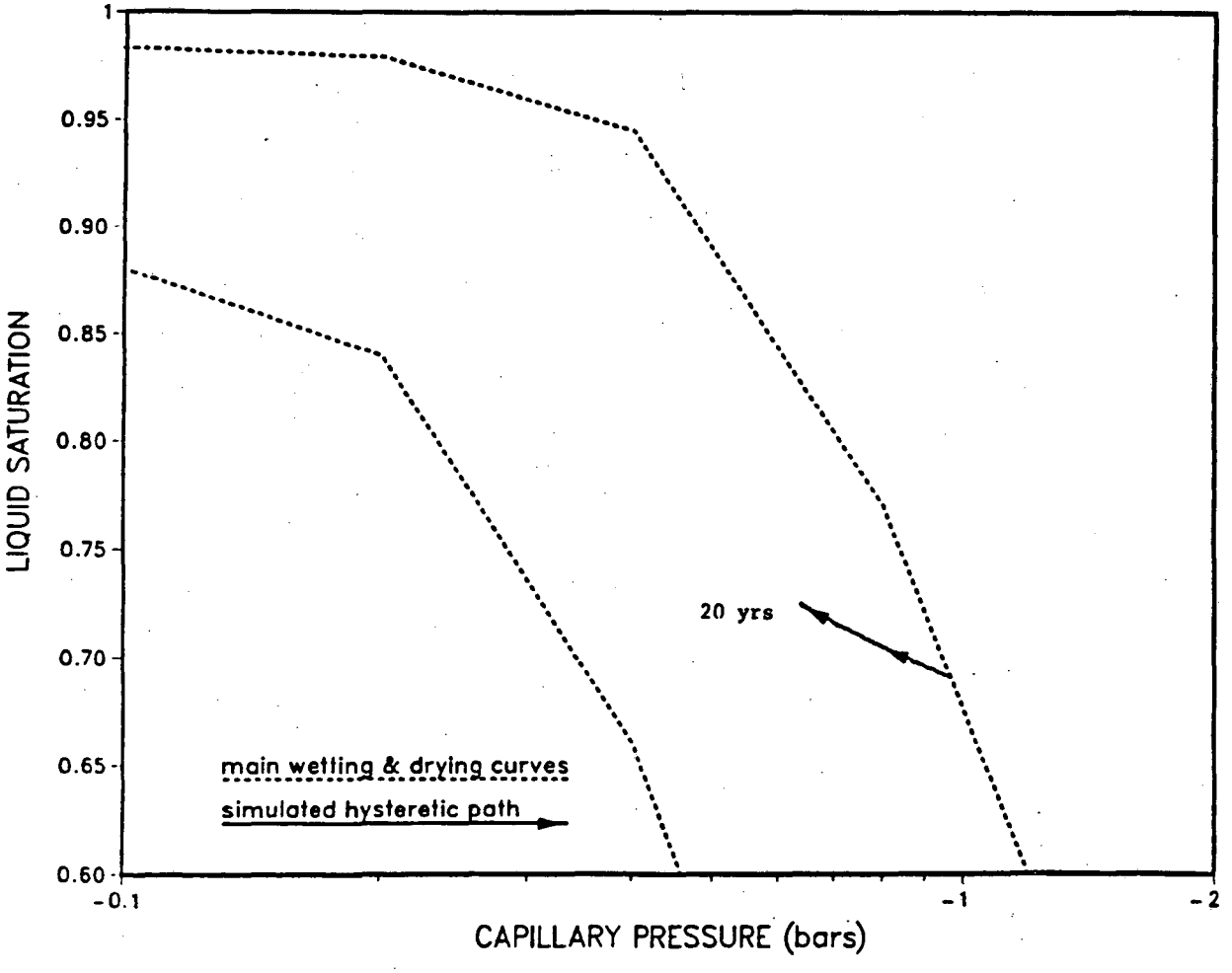

Figure 11d. Model (1): Simulated hysteretic paths for gridblock, center of the matrix, 1.9 m depth.

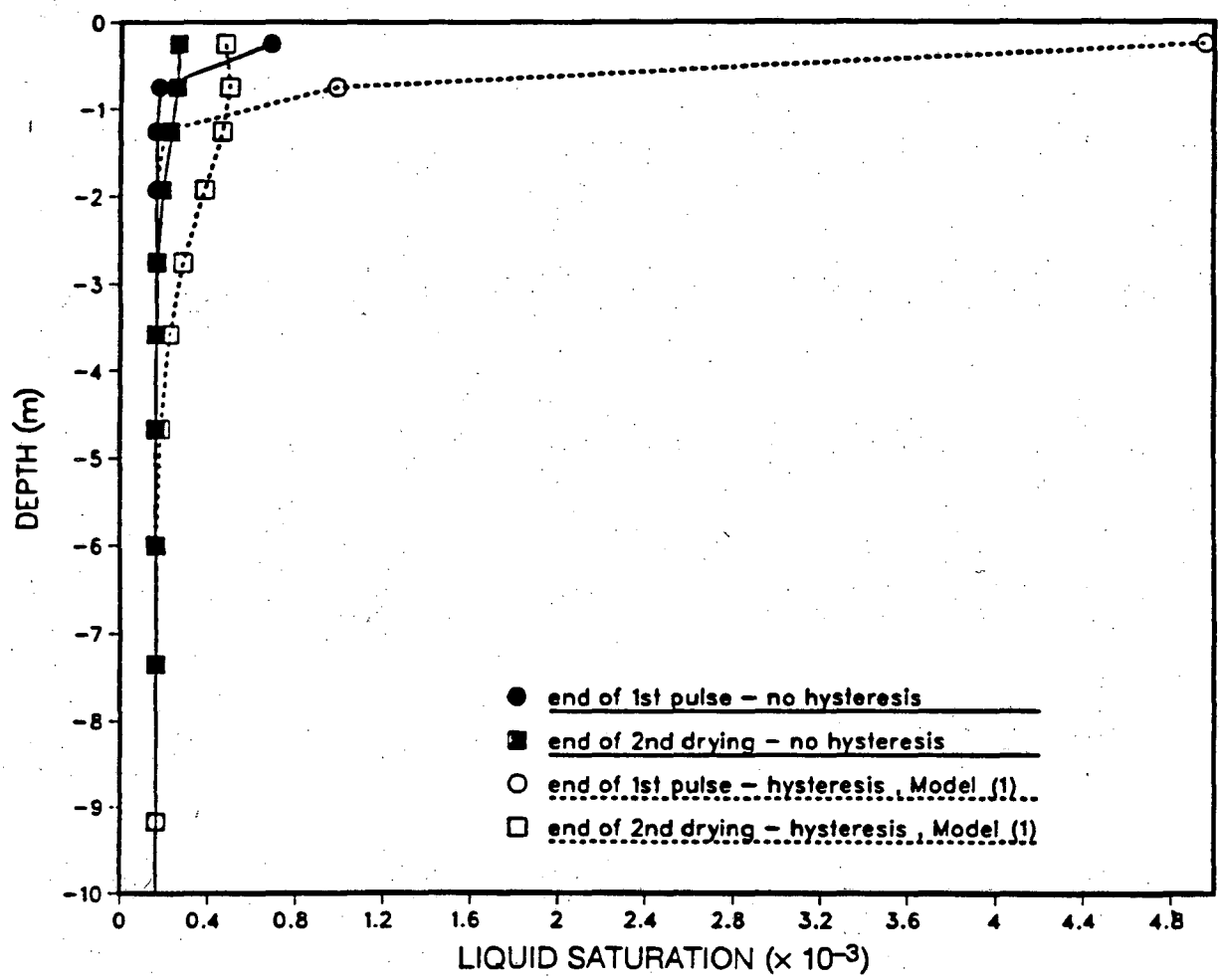

Figure 12. Model (1): Simulated liquid saturations in the fracture.

Consequently, the matrix absorbs less water and more water remains in the fractures.

The fracture liquid saturations remain higher for the hysteretic case throughout the simulation. The liquid saturation distributions at the end of the second recovery show that in the hysteretic case the pulse has penetrated about 2 m deeper than in the non-hysteretic case.

The liquid saturation in the matrix immediately adjacent to the fracture, and in the interior of the matrix, are shown in Figures 13a and 13b, respectively. If the liquid saturation distributions at the end of the second recovery period are compared, it can be seen that the hysteretic case produces a somewhat more "smeared" liquid saturation distribution. In the non-hysteretic case the distribution has a more S-like shape, with a clear front and a more rapid convergence towards the background saturation. This is a result of the combination of higher fracture flow and lower matrix capillary suctions in the hysteretic case. In the non-hysteretic case, with stronger capillary suctions and less water in the fractures, the water is absorbed into the matrix more rapidly and the influence is not felt as deep as in the hysteretic case.

At the end of the second drying periods (at 20 years) the capillary pressures in each layer are practically uniform and the matrix has reached an equilibrium with the adjacent fractures. With capillary pressure equilibrium the matrix liquid saturations are uniform in each layer for the non-hysteretic case. In the hysteretic case matrix saturations are also practically uniform in all layers except the two uppermost ones, where the hysteretic behavior causes the same capillary pressure to correspond to considerably different liquid saturations. Further down, where the reversals from the first-order wetting curve are smaller or non-existent, nearly uniform liquid saturation distributions in each layer result. The horizontal liquid saturation distributions in the uppermost layer for the hysteretic and non-hysteretic cases are shown in Figure 14.

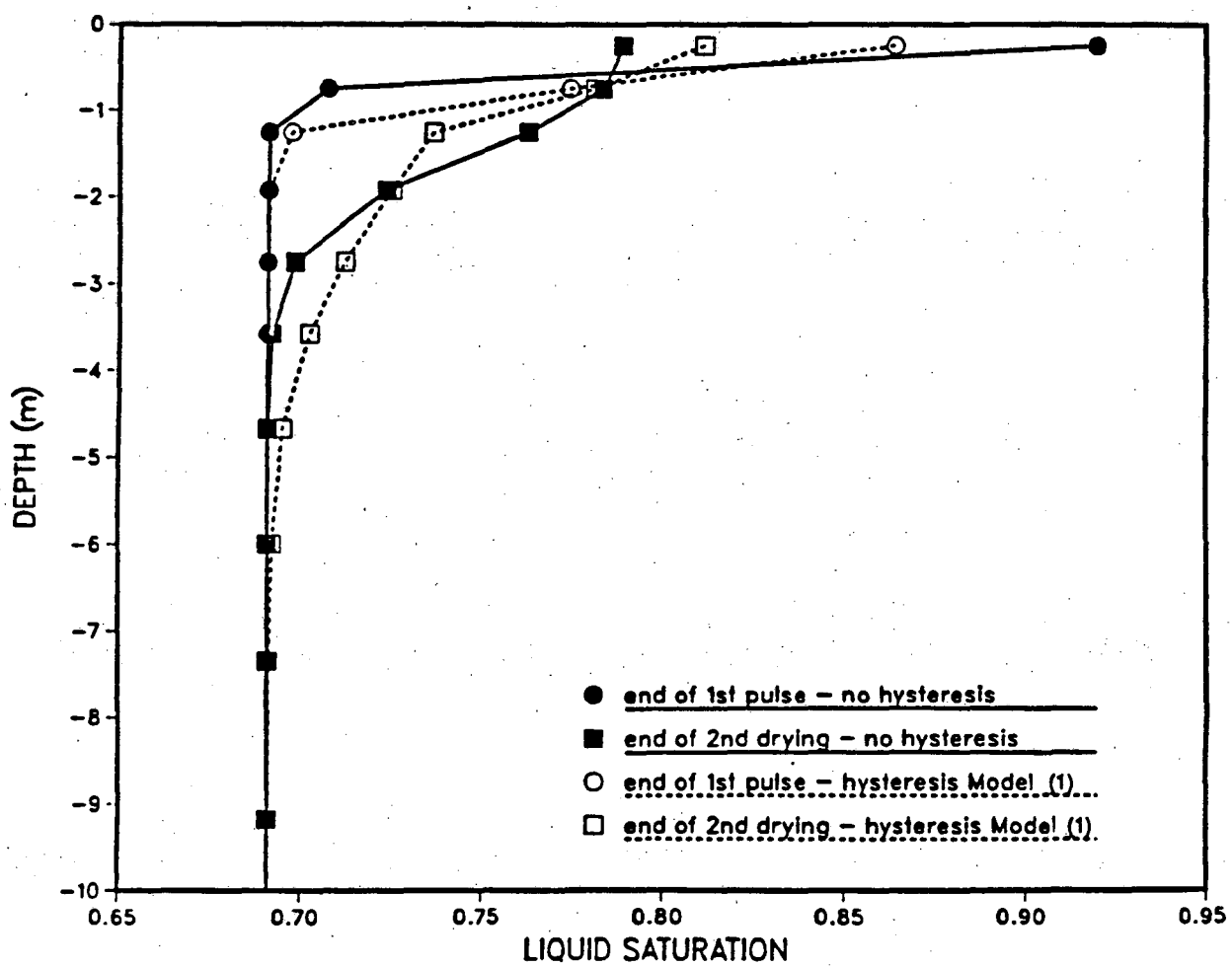

Figure 13a. Model (1): Simulated liquid saturations for the matrix cross-section at 0.5 mm distance from the fracture.

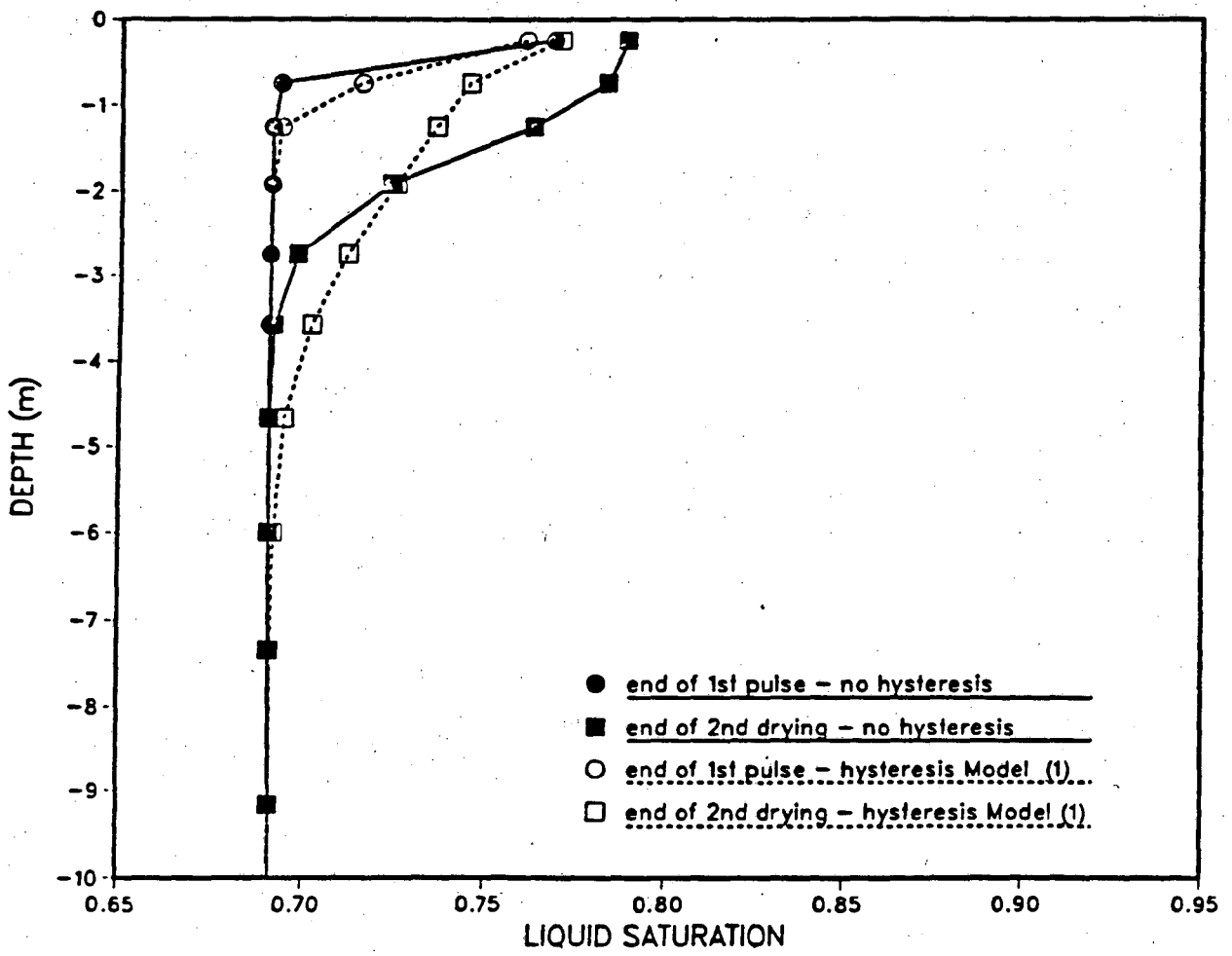

Figure 13b. Model (1): Simulated liquid saturations for the matrix cross-section in the center of the matrix.

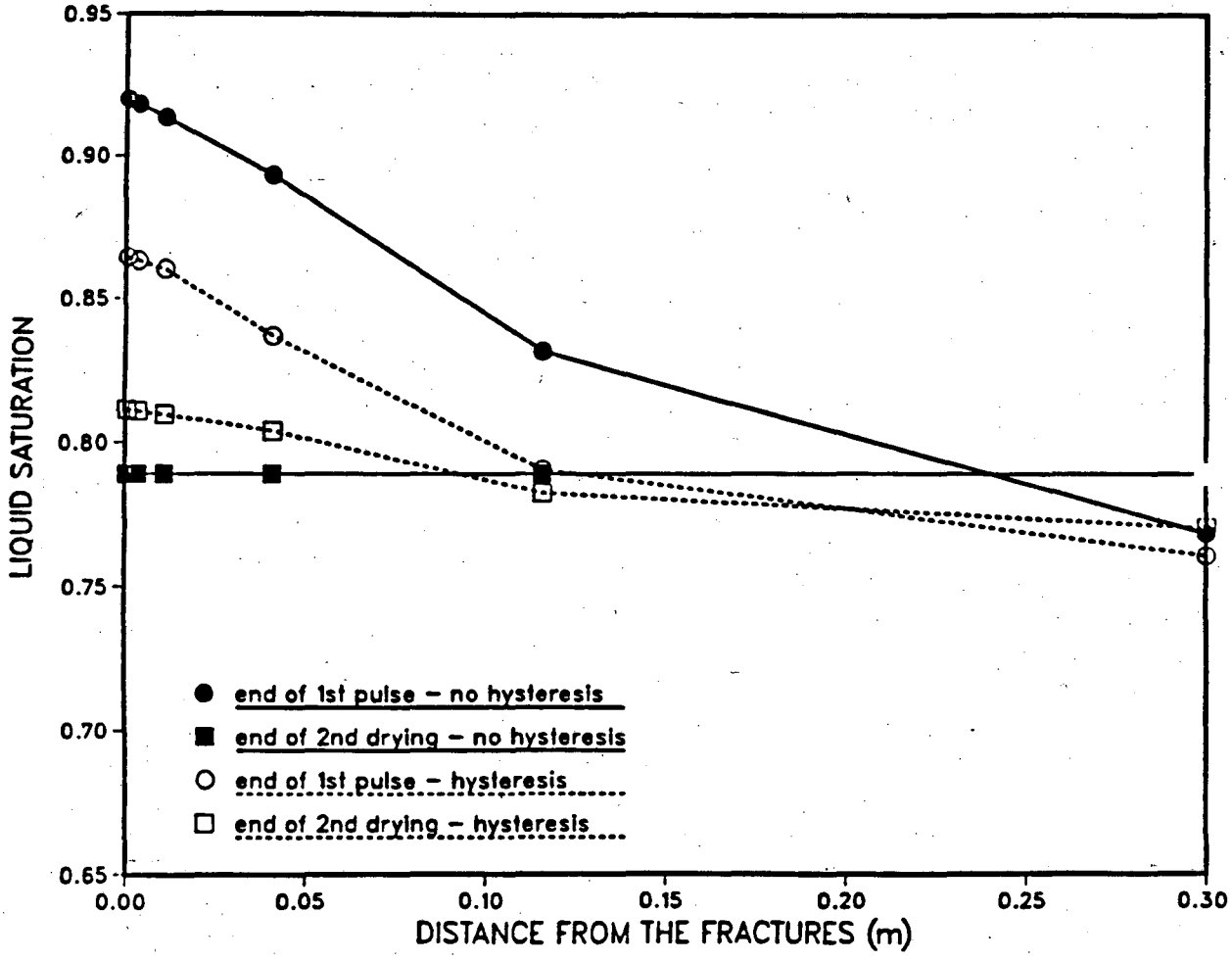

Figure 14. Model (1): Simulated liquid saturation in the matrix at 0.25 m depth.

5.4. Simulations with Model (2) (Ten-year Cycle)

The problem solved with model (1) in the previous section is solved using model (2) in this section. The main wetting and drying curves shown in Figure 10 are used, and the scanning paths are solved internally using the equations given in Section 3.2.

Simulated hysteretic paths for some matrix elements during one pulse cycle are shown in Figures 15a through 15d. Simulated liquid saturation distributions in the fractures and in the adjacent matrix at the end of the first pulse (3 months) and at the end of the first drying period (10 yrs) are shown in Figures 16 and 17; the corresponding results obtained with model (1) are also shown in these figures.

With model (2), the simulation could not be continued beyond the end of the first drying period. At the beginning of the second wetting period serious convergence problems and continuous phase transitions occurred in the uppermost fracture element (element adjacent to the element shown in Figure 15a), preventing the reversal from drying to wetting. This is most likely a result of the discontinuity of the scanning path at the reversal from second-order drying back to wetting. As discussed in Section 3.2, in model (2) no separate expressions are used for third- and higher-order scanning curves, and upon reversal from second-order drying back to wetting the process "jumps" back to the first-order wetting curve. This approximation, suggested by Killough (1976), was used in order to maintain the simplicity of the model without generating significant errors. In the case of the element in Figure 15a, however, this "jump" corresponds to a very significant change in capillary pressure (from ≈ .7 bars to ≈ .4 bars). Because the adjacent fracture element has a very small volume and contains small amounts of water, this kind of drastic changes in the neighboring element can generate serious convergence problems.

Since the first-order scanning curves used for model (1) (Figure 10), were originally derived using Equations (1) and (2), which internally compute the scanning curves for model (2), comparisons between the results obtained with the two models can be made.

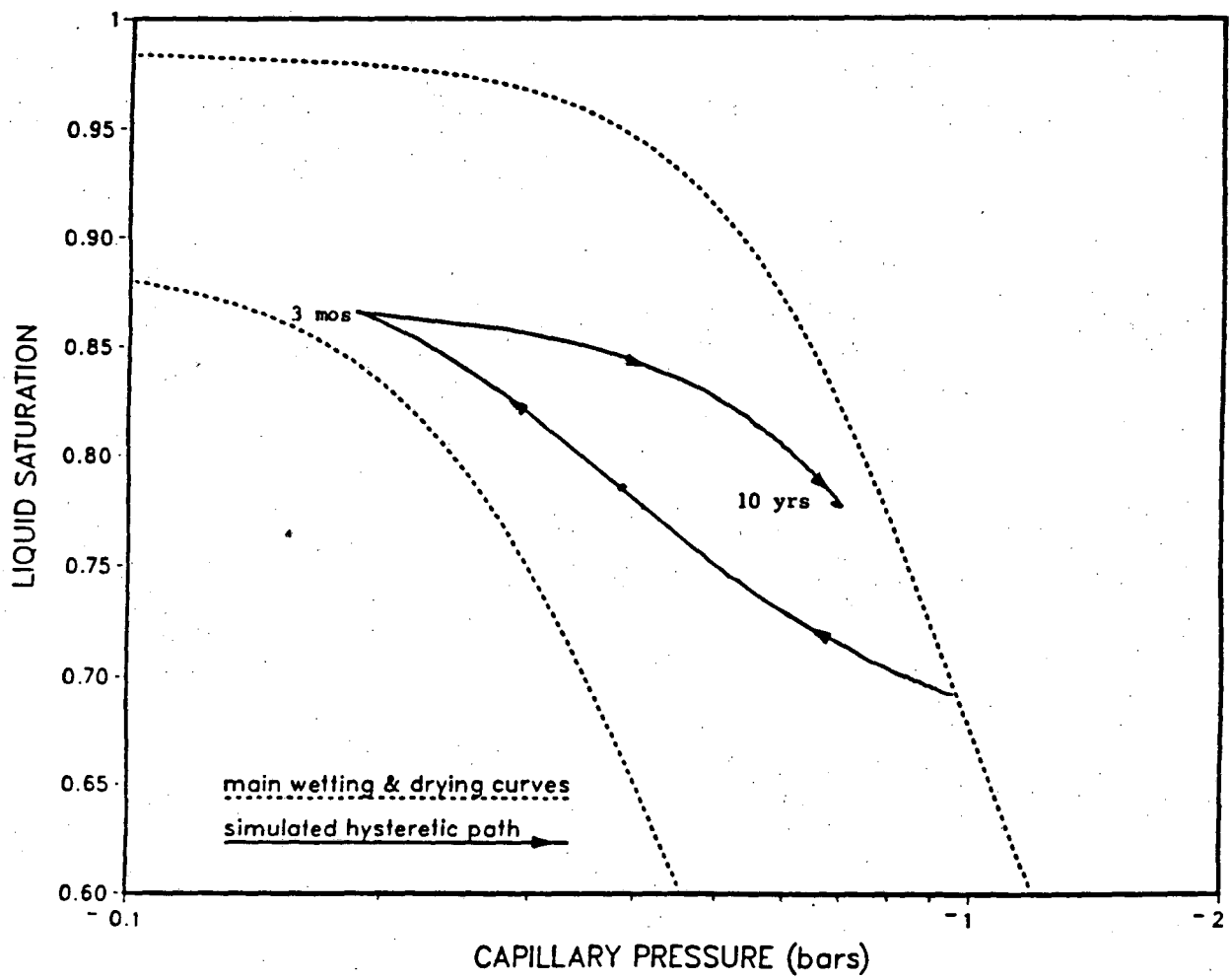

Figure 15a. Model (2): Simulated hysteretic paths for gridblock, 0.5 mm from the fracture, 0.25 m depth.

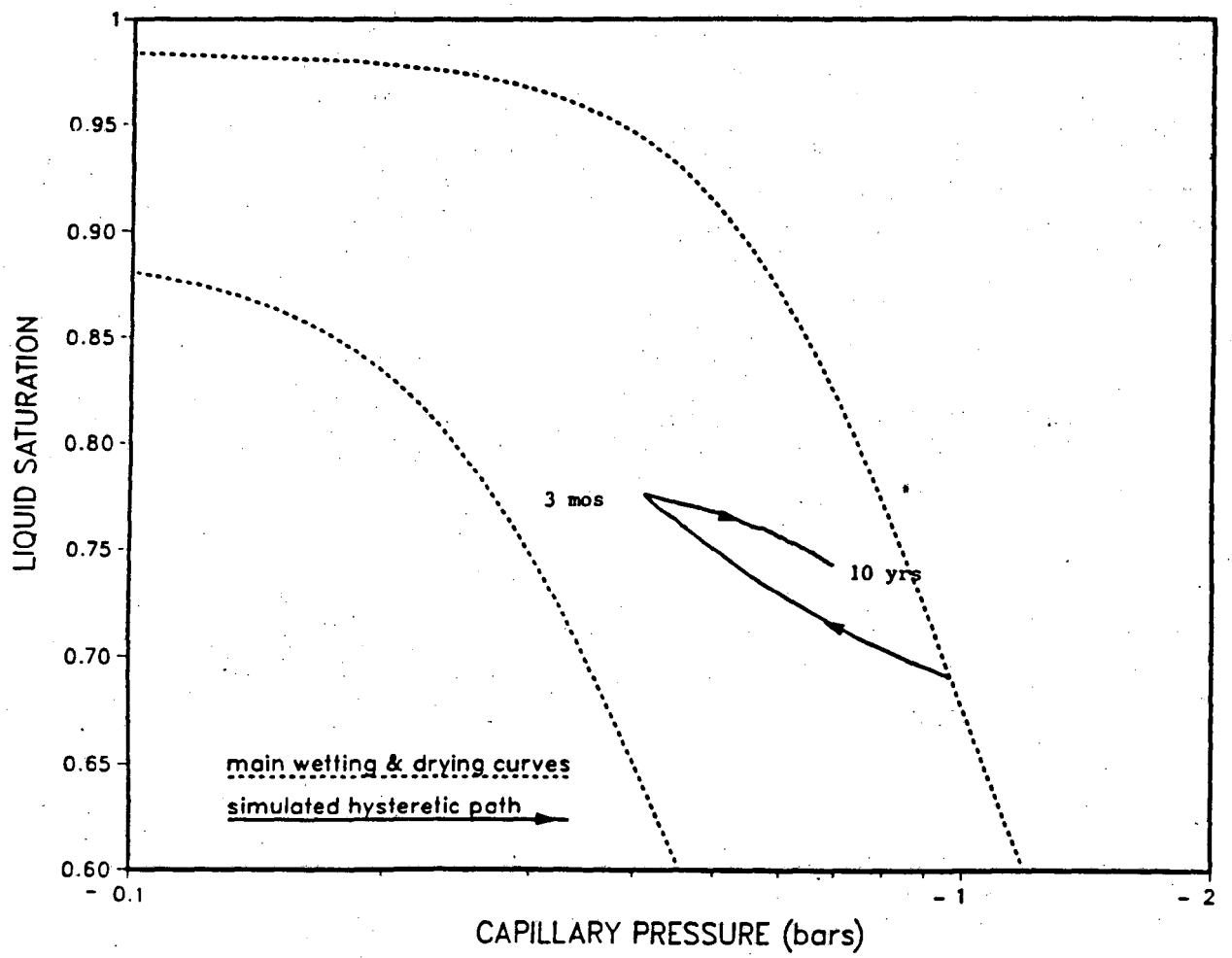

Figure 15b. Model (2): Simulated hysteretic paths for gridblock, center of the matrix, 0.25 m depth.

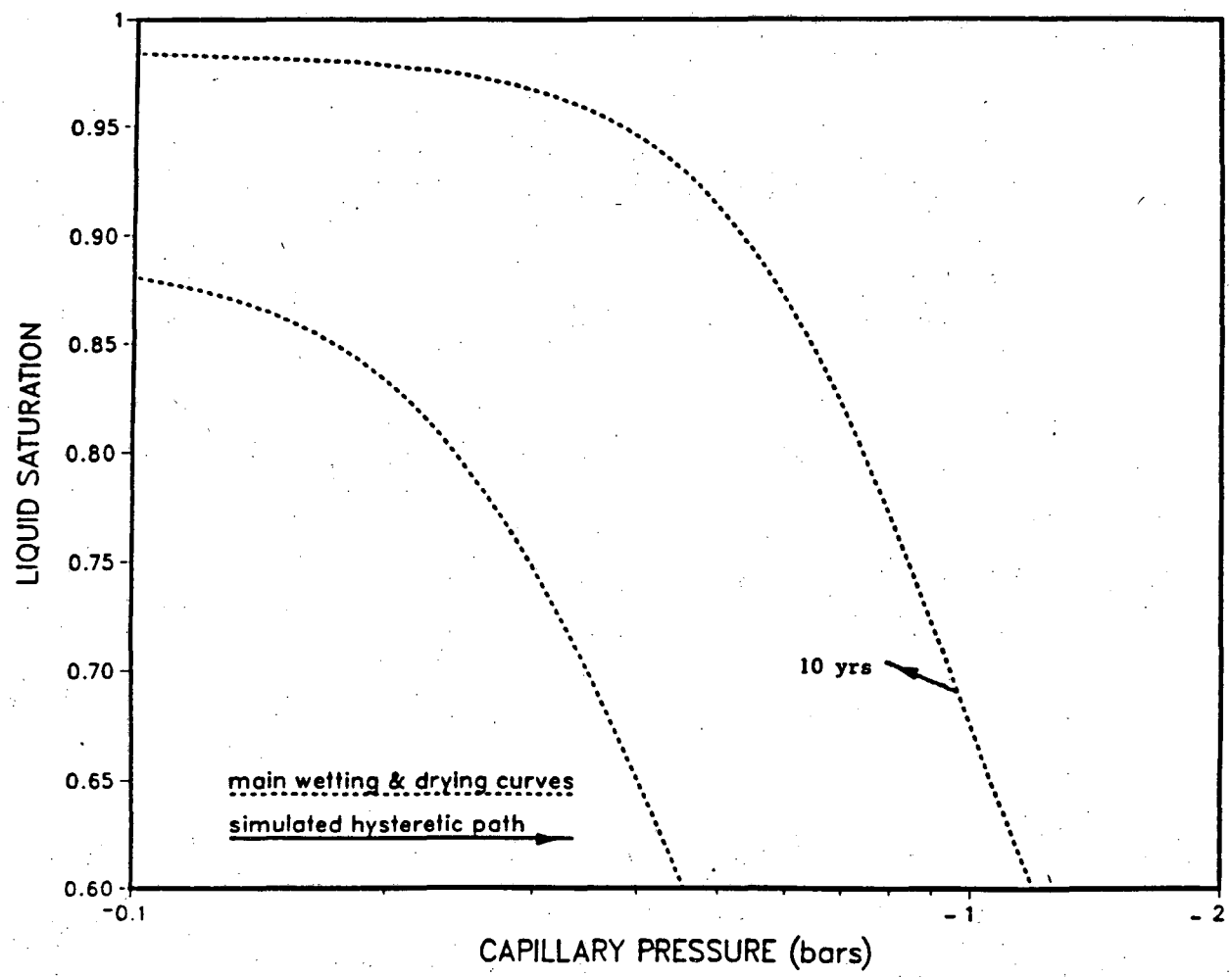

Figure 15c. Model (2): Simulated hysteretic paths for gridblock, 0.5 mm from the fracture, 1.9 m depth.

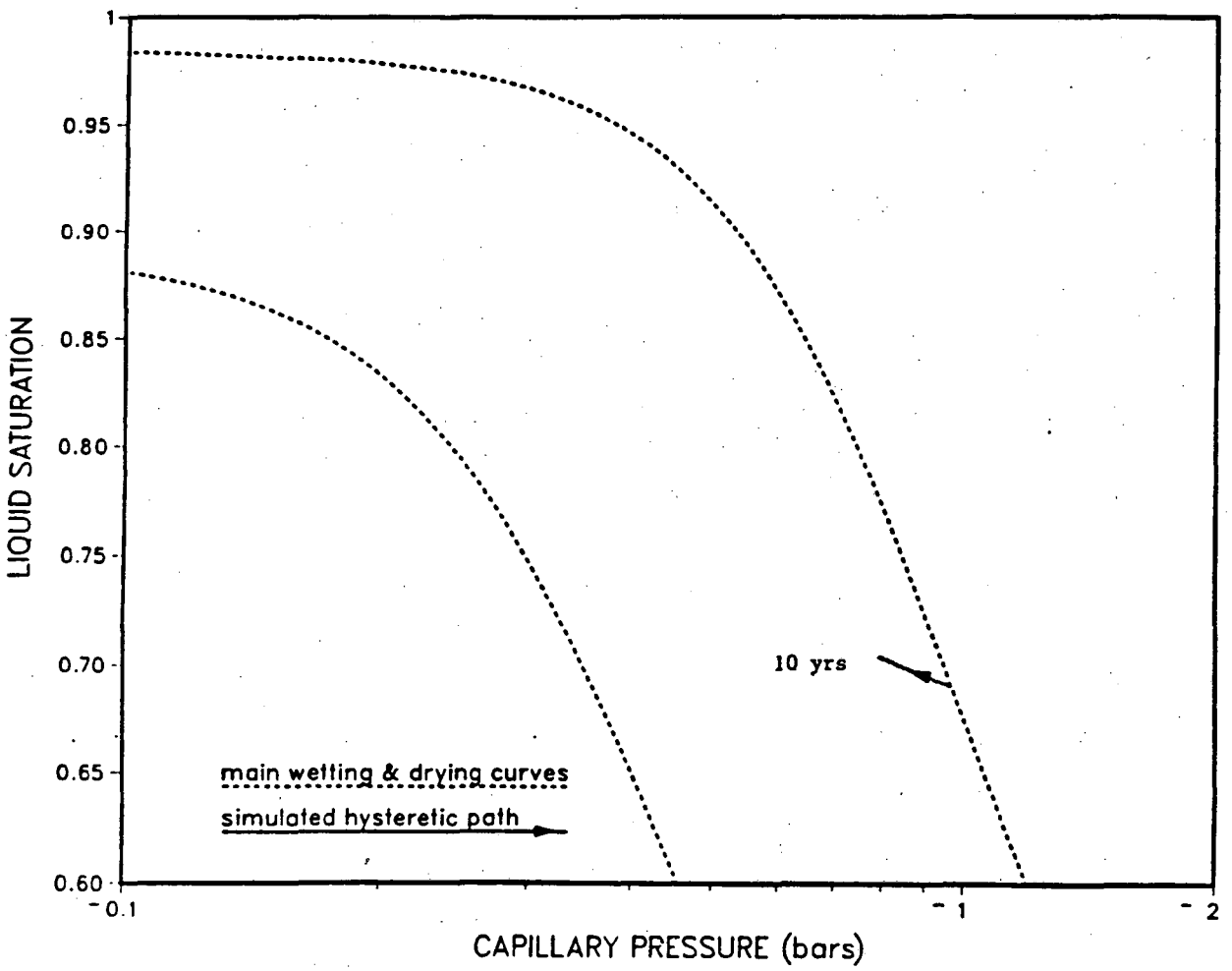

Figure 15d. Model (2): Simulated hysteretic paths for gridblock, center of the matrix, 1.9 m depth.

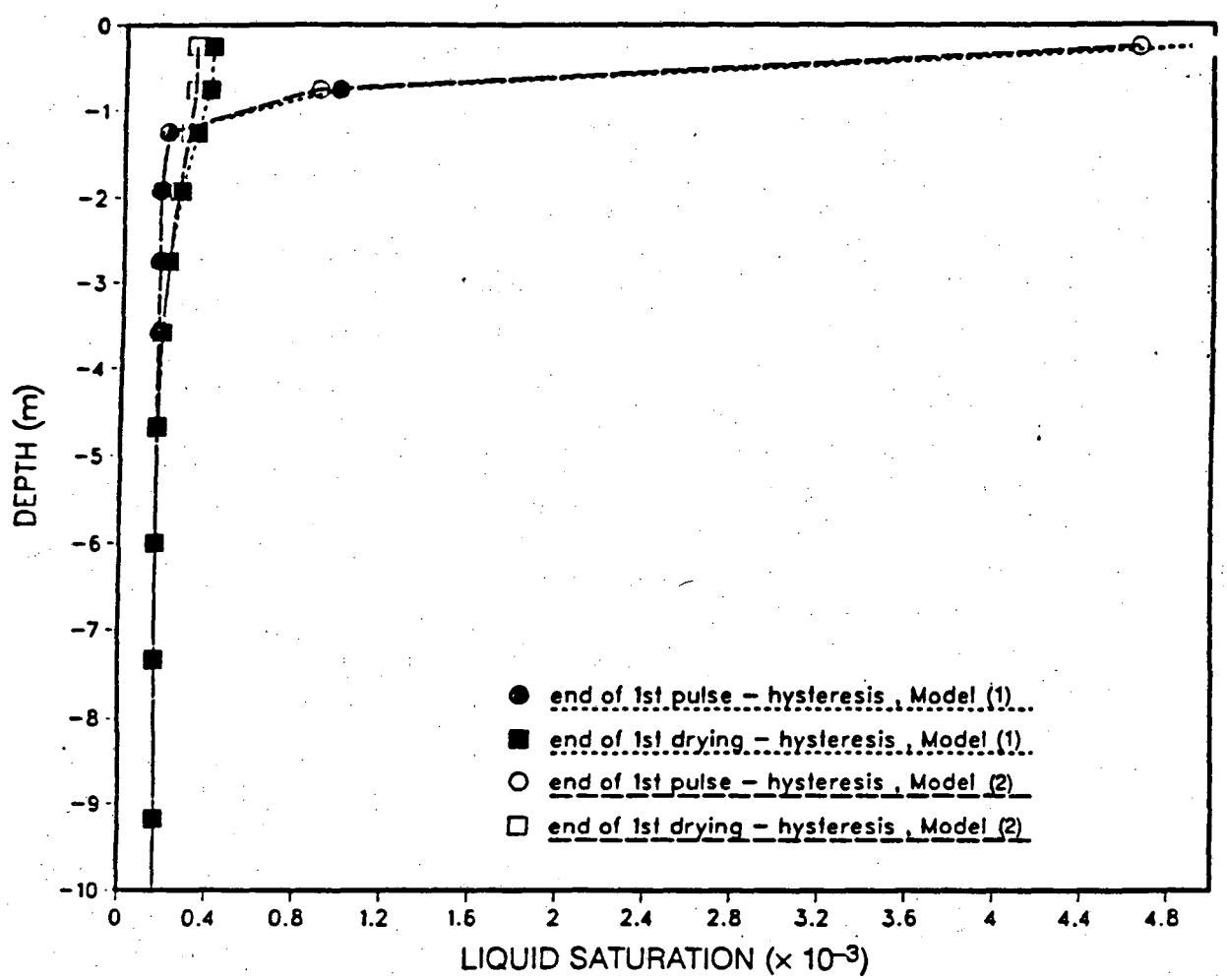

Figure 16. Model (2) versus model (1): Simulated liquid saturations in the fracture.

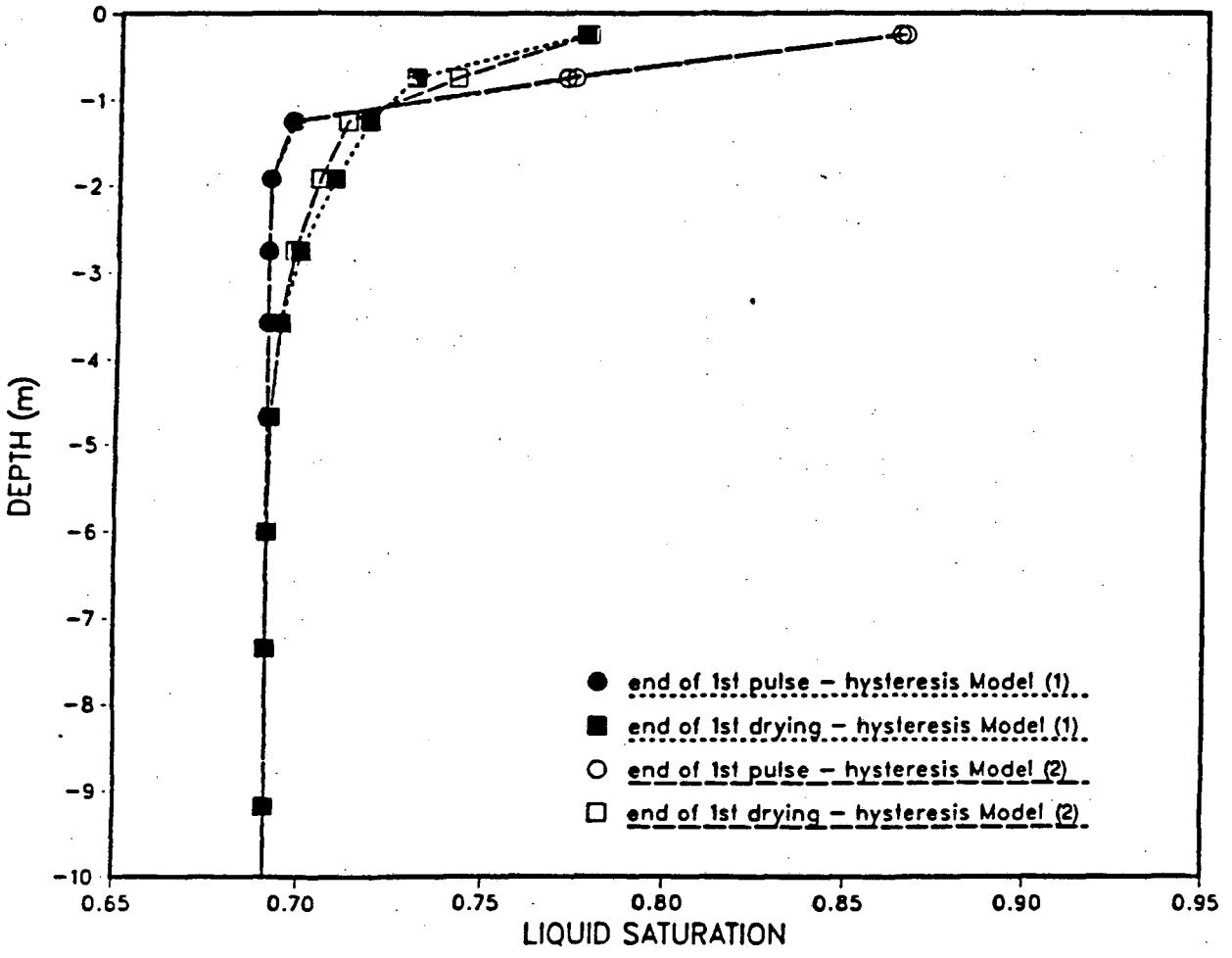

Figure 17. Model (2) versus model (1): Simulated liquid saturations for the matrix cross-sections at 0.5 mm distance from the fracture.

As can be seen by examining Figures 16 and 17, the results after the first pulse are practically identical. The similarity of the predictions during the first wetting period can also be seen by comparing Figures 11a through 11d with Figures 15a through 15d.

At the end of the first drying period the liquid saturation distributions are somewhat different. This difference is a result of the inaccuracy generated by model (1) due to the fact that the second-order drying curves are approximated by the tabulated first-order curves. These curves converge towards the minimum saturation (see Figure 10), whereas in model (2) the second-order curves converge towards the point on the main drying curve from which the original reversal took place. This "pumping" effect of model (1) results in slight overprediction of the hysteresis effects in the upper layers. However, similar "smearing" of the moisture front can be seen in the predictions for both models, and the pulse penetration depths are also similar.

The convergence problems that occurred with model (2) in the beginning of the second wetting period obviously demonstrate a weakness of this model. These problems can be easily avoided by giving separate expressions for the third- and higher-order scanning curves, for example in a manner similar to that we have used for model (3). It appears, however, that this particular convergence problem was very sensitive to the material properties used. When the system described earlier was solved with only slightly different properties, these convergence problems did not occur. In this other study all other parameter values were those shown in Table 2, except that a 1 mm volumetric aperture and a 0.1 porosity were assumed for the fracture (resulting in a somewhat over-estimated fracture flow). For the $k_{rl} = k_{rl}(S_l)$ relation for the matrix the equation shown in Table 1 was used, rather than that shown in Table 2. The mesh used was similar to that shown in Figure 8 except that three times coarser discretization was used in the vertical direction (uppermost element 1.5 m thick in comparison 0.5 m used earlier). The mesh was also longer due to the greater expected penetration depth of the pulse. The simulated hysteretic path for the matrix element closest to the top and adja-

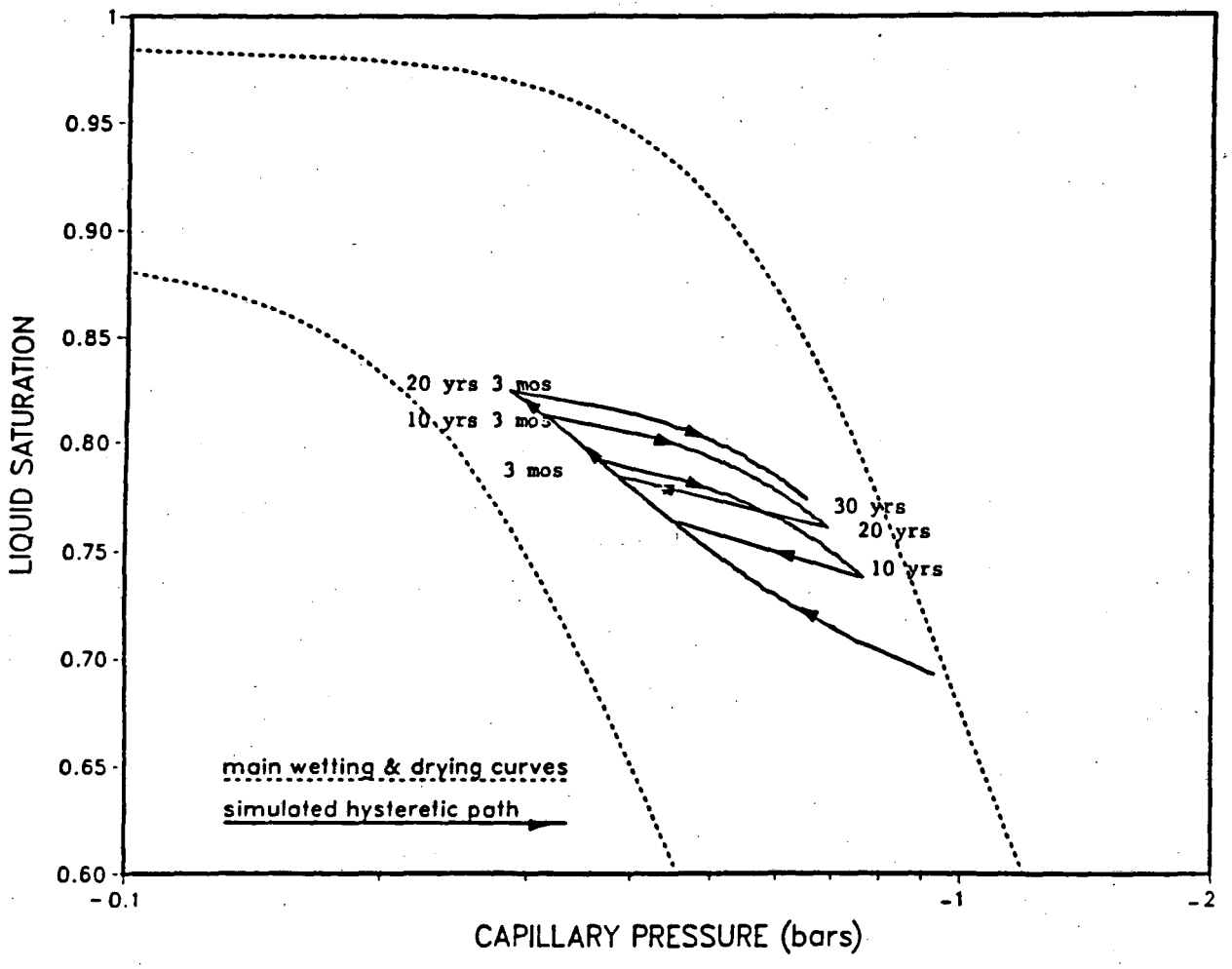

Figure 18. Model (2) (1 mm volumetric aperture for the fracture): Simulated hysteretic path for the grid block at 0.5 mm from the fracture and 0.75 m depth.

cent to the fracture obtained with these parameters is shown in Figure 18.

5.5. Simulations with Model (3) (Ten-Year Cycle)

In this set of simulations the problem earlier solved with models (1) and (2) is solved using model (3). For this set of simulations curve (3) in Figure 9 was used as the main wetting curve.

Simulated hysteretic paths for the trace elements used in the earlier examples are shown in Figures 19a through 19d. Due to the structure of model (3), "pumping" can not take place at any level of the scanning curve order. Convergence problems such as those encountered with model (2), do not occur because of the way we have treated the higher than second-order scanning curves. Figures 20, 21a,b and 22 show the simulated liquid saturations at the end of the first pulse and the second drying period for both the hysteretic and non-hysteretic cases. "Smearing" of the liquid saturation distribution observed in the earlier cases can be seen in these figures as well. For the fracture, the pulse has penetrated about 1-2 m deeper in the hysteretic case than in the non-hysteretic case. The strongly hysteretic behavior is limited to the uppermost layers and below the third layer the system is continuously wetting along the first-order wetting curves. At the end of both drying periods the capillary pressures are uniform and in equilibrium with adjacent fractures. In the uppermost layer this corresponds to a non-uniform liquid saturation distribution, as shown in Figure 22. The maximum local difference in the final liquid saturations between the hysteretic and non-hysteretical cases is ≈4%. Because the derivation of model (3), unlike those of models (1) and (2), is based on theoretical presentation of hysteresis rather than empirical results, predictions from this model can probably be considered most reliable until actual hysteresis data for the welded units become available. Keeping in mind that the main wetting curve used is derived by using information from soil literature, one can probably look at these results as first-order estimates of the possible hysteresis effects in a fracture-rock matrix system.

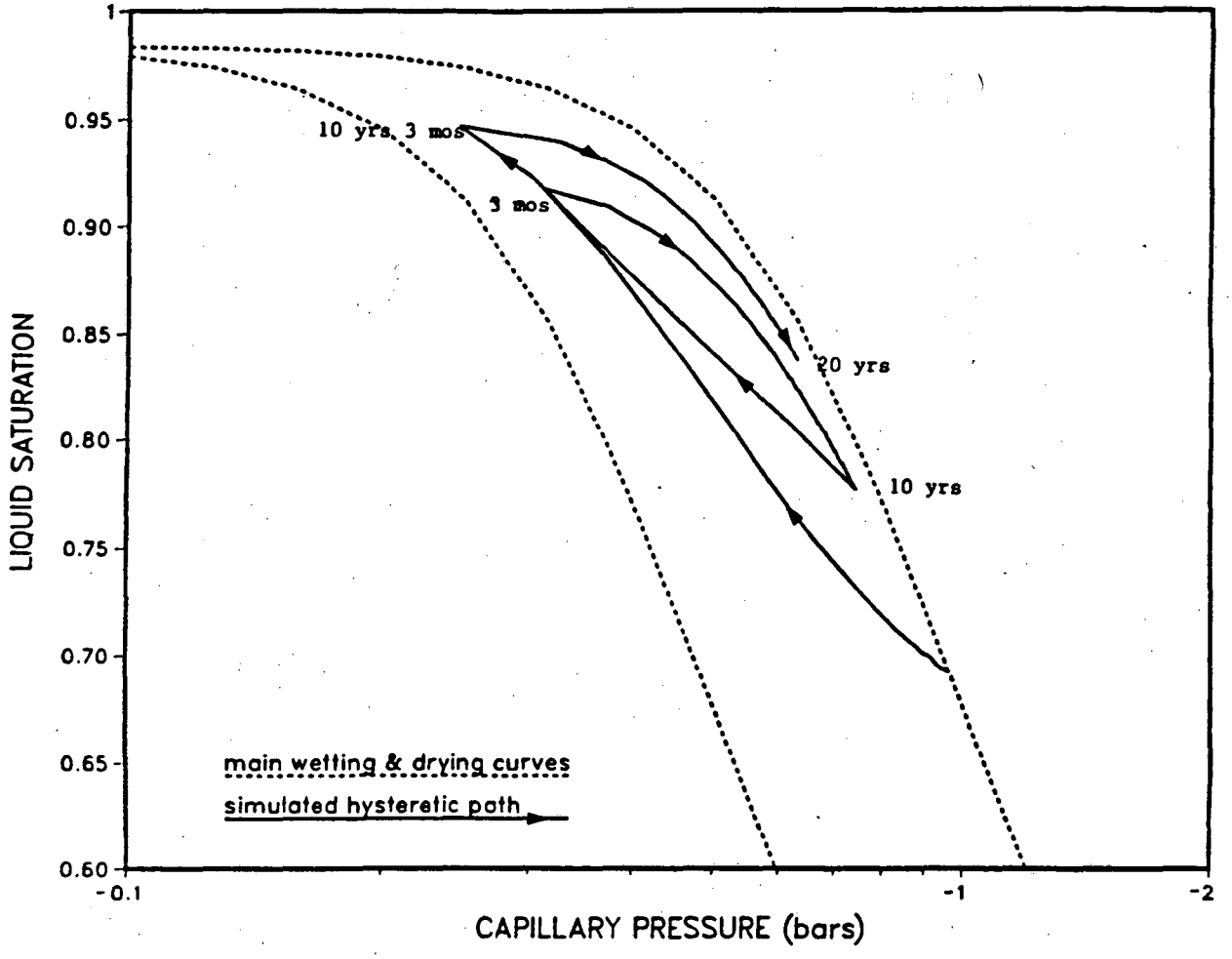

Figure 19a. Model (3): Simulated hysteretic paths for gridblock, 0.5 mm from the fracture, 0.25 m depth.

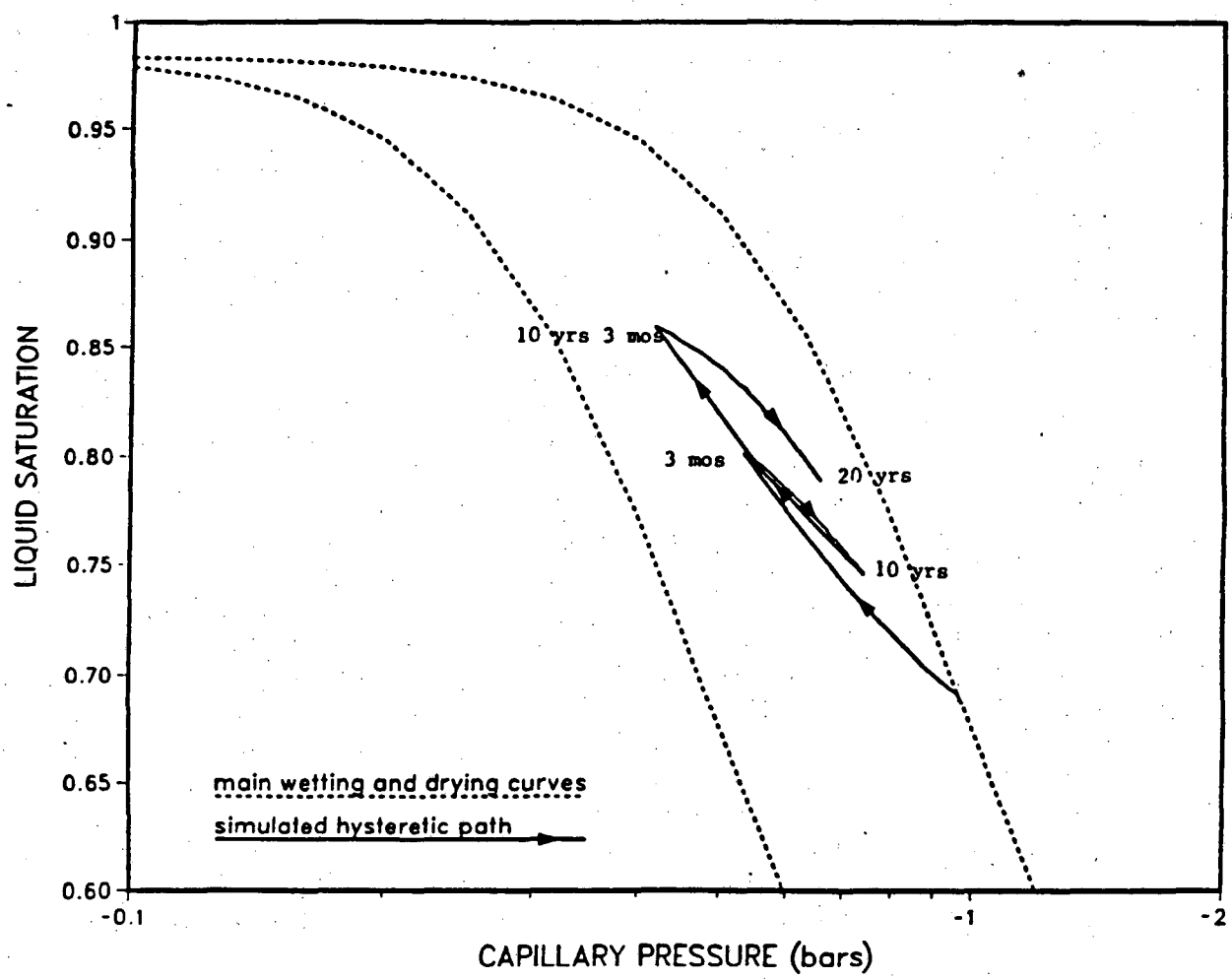

Figure 19b. Model (3): Simulated hysteretic paths for gridblock, center of the matrix, 0.25 m depth.

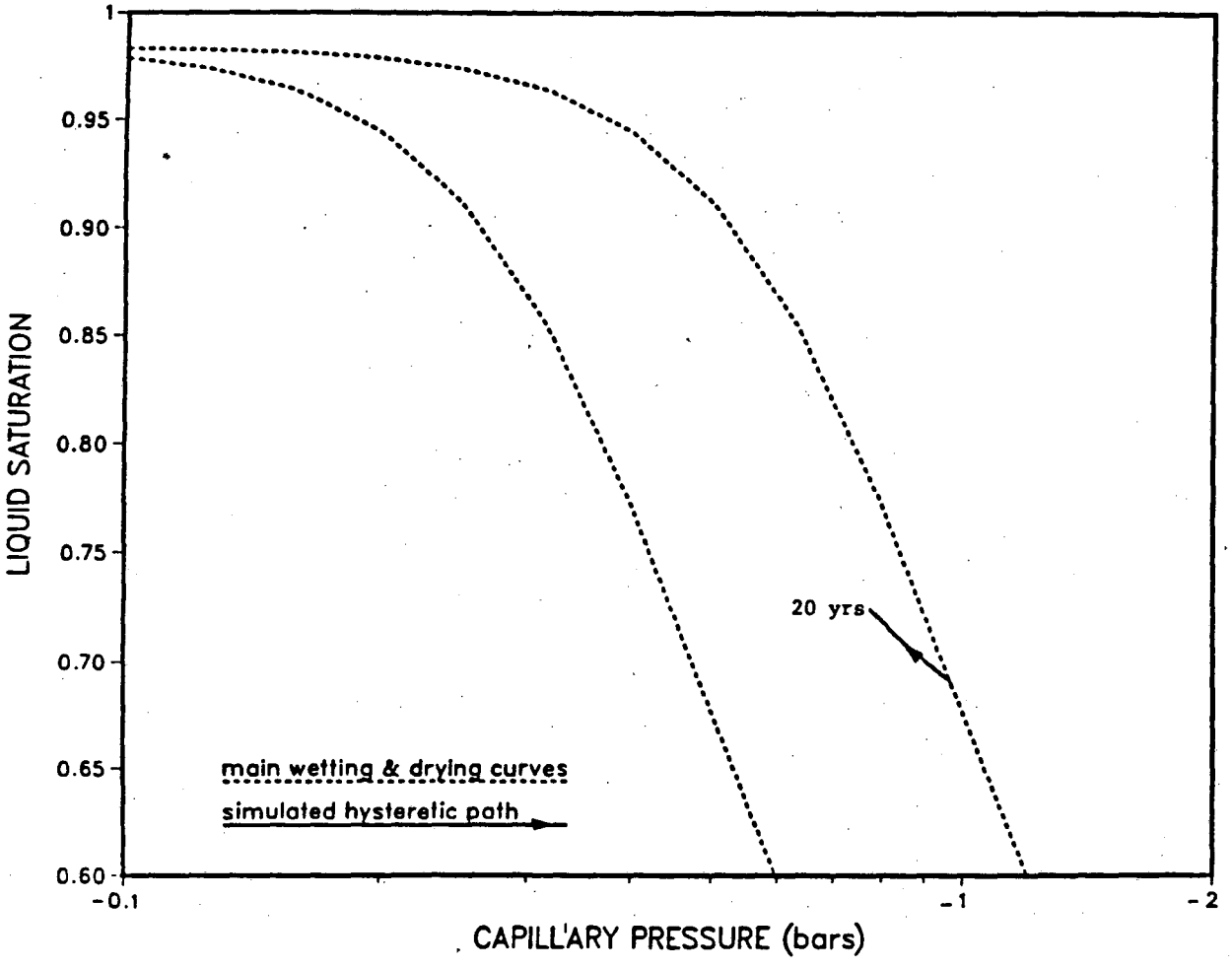

Figure 19c. Model (3): Simulated hysteretic paths for gridblock, 0.5 mm from the fracture, 1.9 m depth.

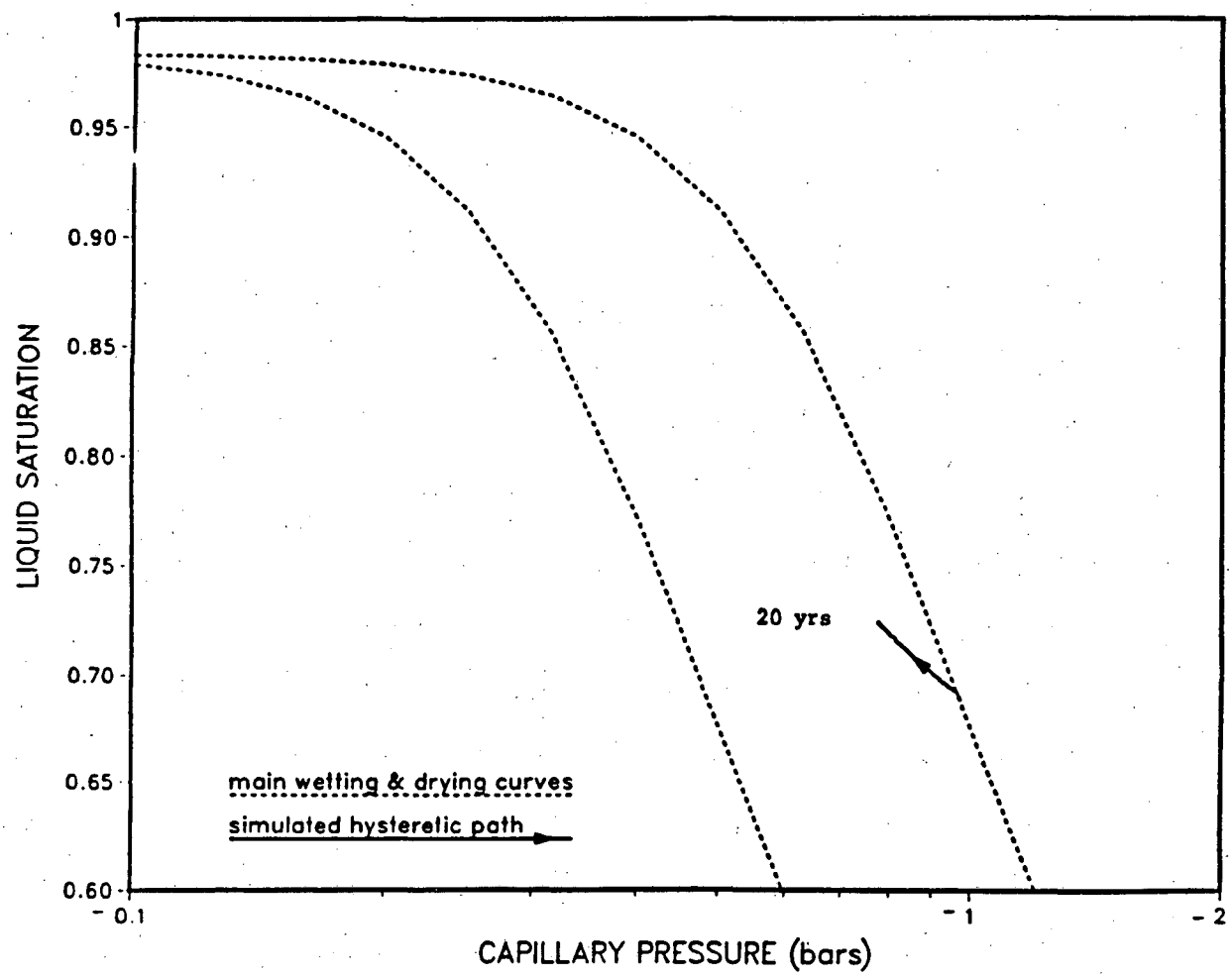

Figure 19d. Model (3): Simulated hysteretic paths for gridblock, center of the matrix, 1.9 m depth.

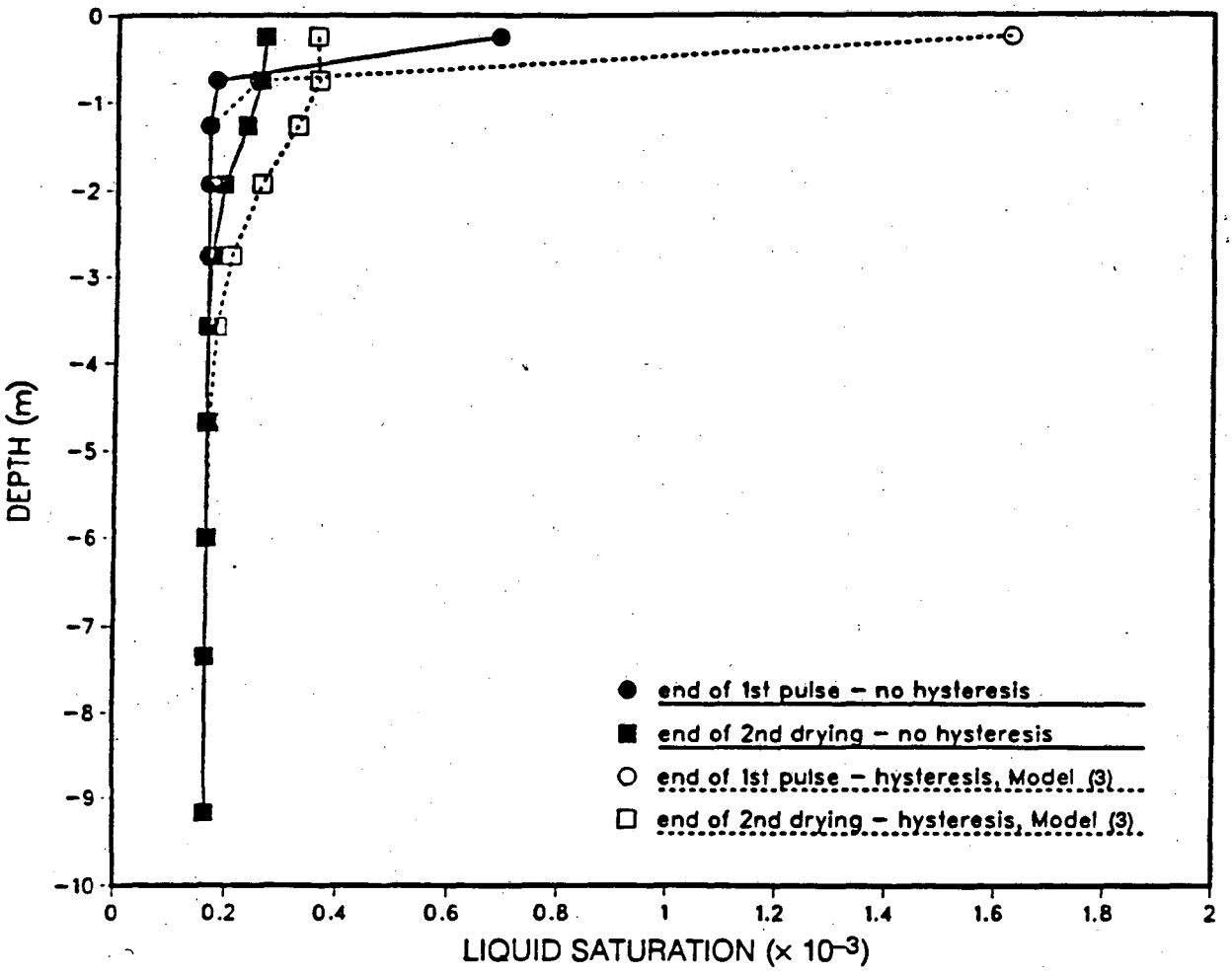

Figure 20. Model (3): Simulated liquid saturations in the fracture.

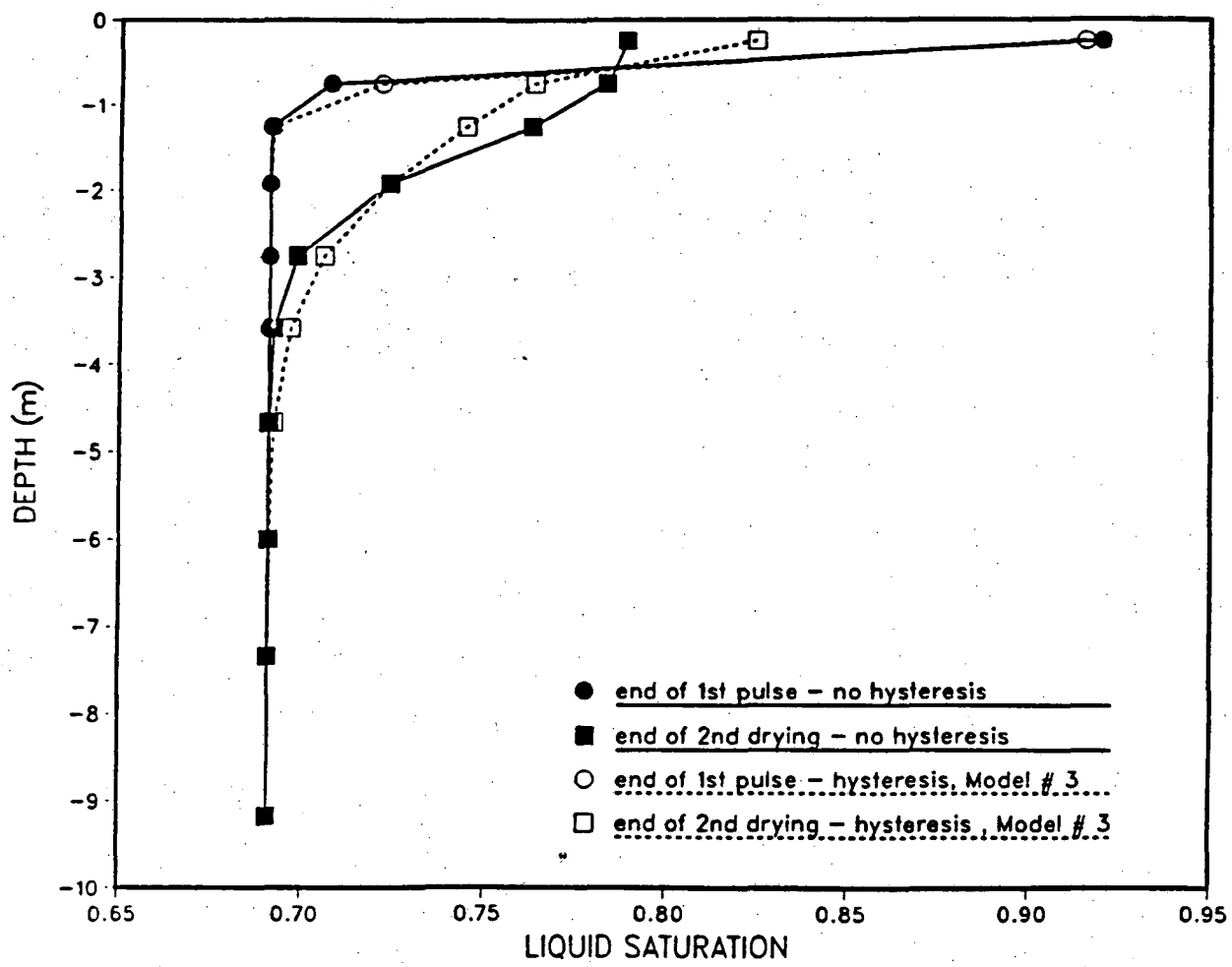

Figure 21a. Model (3): Simulated liquid saturations for the matrix cross-section at 0.5 mm distance from the fracture.

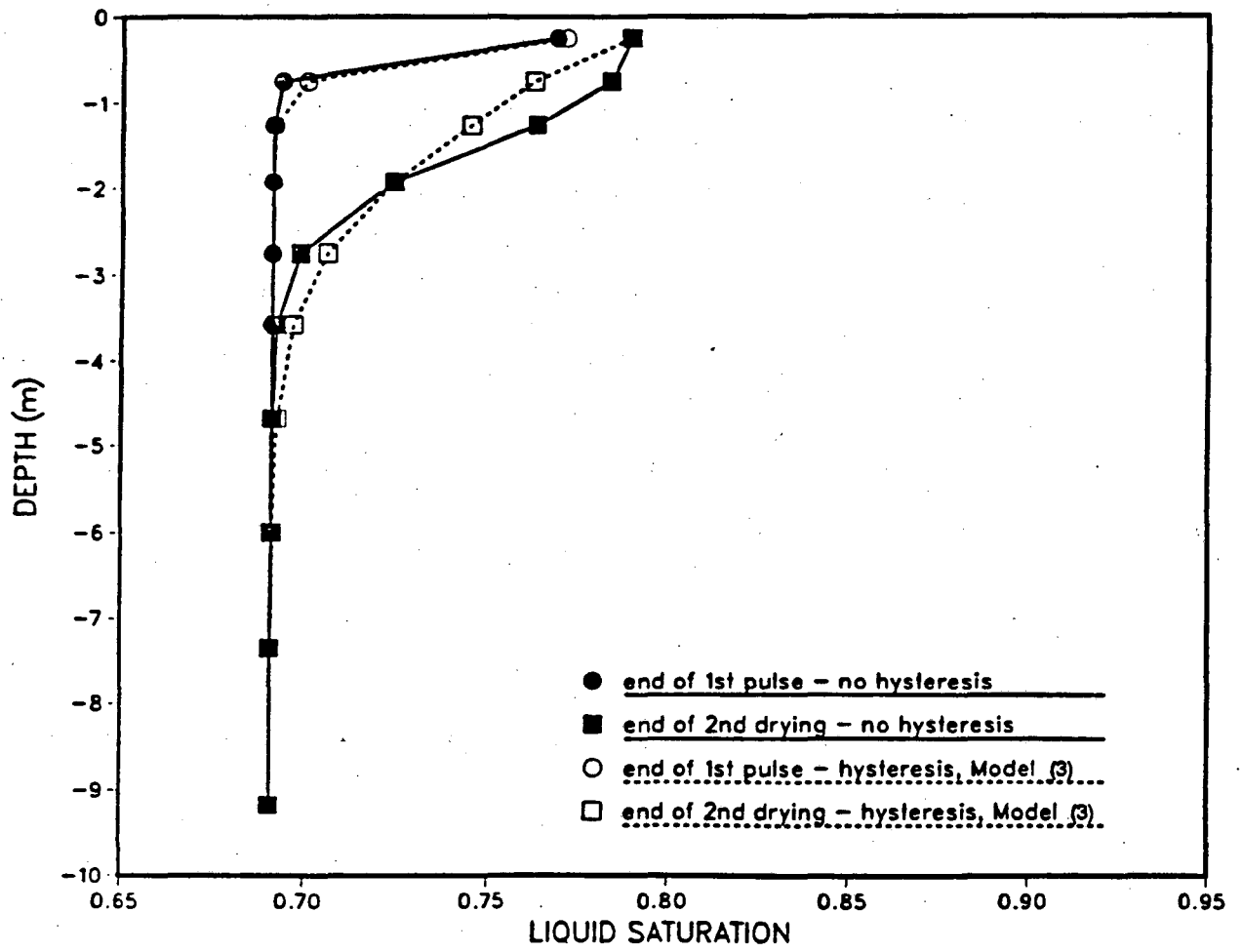

Figure 21b. Model (3): Simulated liquid saturations for the matrix cross-section in the center of the matrix.

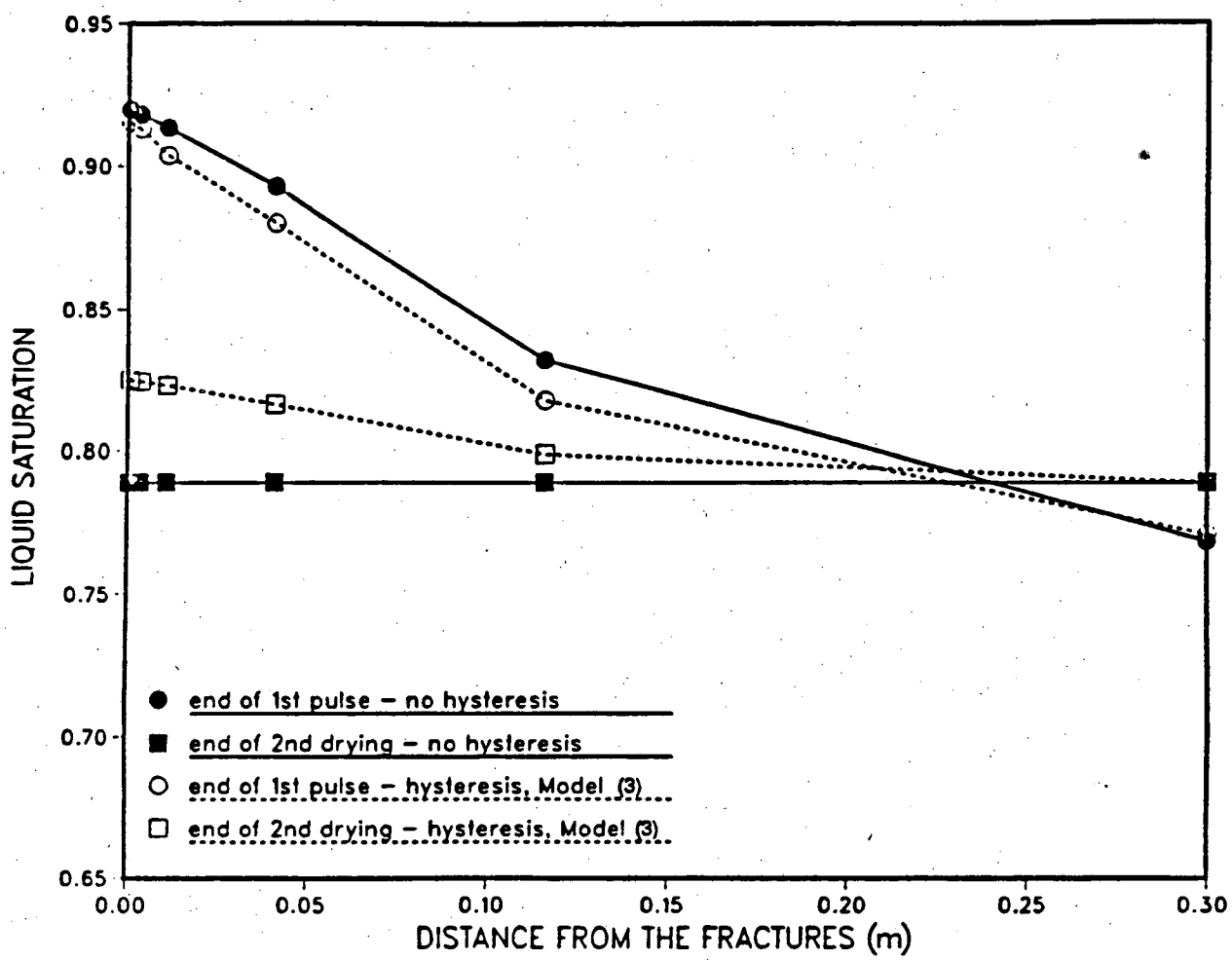

Figure 22. Model (3): Simulated liquid saturations for the matrix at 0.25 m depth.

5.6. Simulations with One-Year Cycle

One set of simulations was carried out by assuming an intensive annual rain period. For each one-year cycle a pulse infiltration corresponding to 1 mm/yr precipitation concentrated into a three-month period (1 mm/yr x 1 yr/0.25 yr = 4 mm/yr) was introduced for three months. This pulse was followed by a nine-month drying period during which the background precipitation of 0.1 mm/yr was assumed. The cycle was repeated eight times and the system was first modeled without capillary hysteresis and then with hysteresis, using models (1) and (2).

The parameter values used were similar to those shown in Table 2 except that the matrix $k_{rl} = k_{rl}(S)$ was that given in Table 1, and for the fracture a volumetric aperture of 1 mm and a porosity of 0.1 were used. The mesh used was similar to that shown in Figure 8 except that a three times coarser vertical discretization was used.

The resulting matrix liquid saturations after eight years are shown in Figures 23a and 23b. As can be seen from these figures, the overall pulse effects are very small. With this pulse the liquid saturation in the uppermost layer in the interior of the matrix oscillates between wetting and drying, but drying is so unsignificant that the hysteretic paths appear to be almost monotonically increasing.

Adjacent to the fracture the changes in liquid saturation are significant enough to produce clear reversals, but are too small to produce looplike scanning paths for model (1), which produces a very pronounced pumping effect as seen in Figure 24a. The corresponding path obtained with model (2) is shown in Figure 24b. Due to the pumping effect the predictions of the two models are very different near the fracture (Figure 23a) and also rather different in the interior of the matrix, considering that the overall hysteresis effects are rather small (Figure 23b).

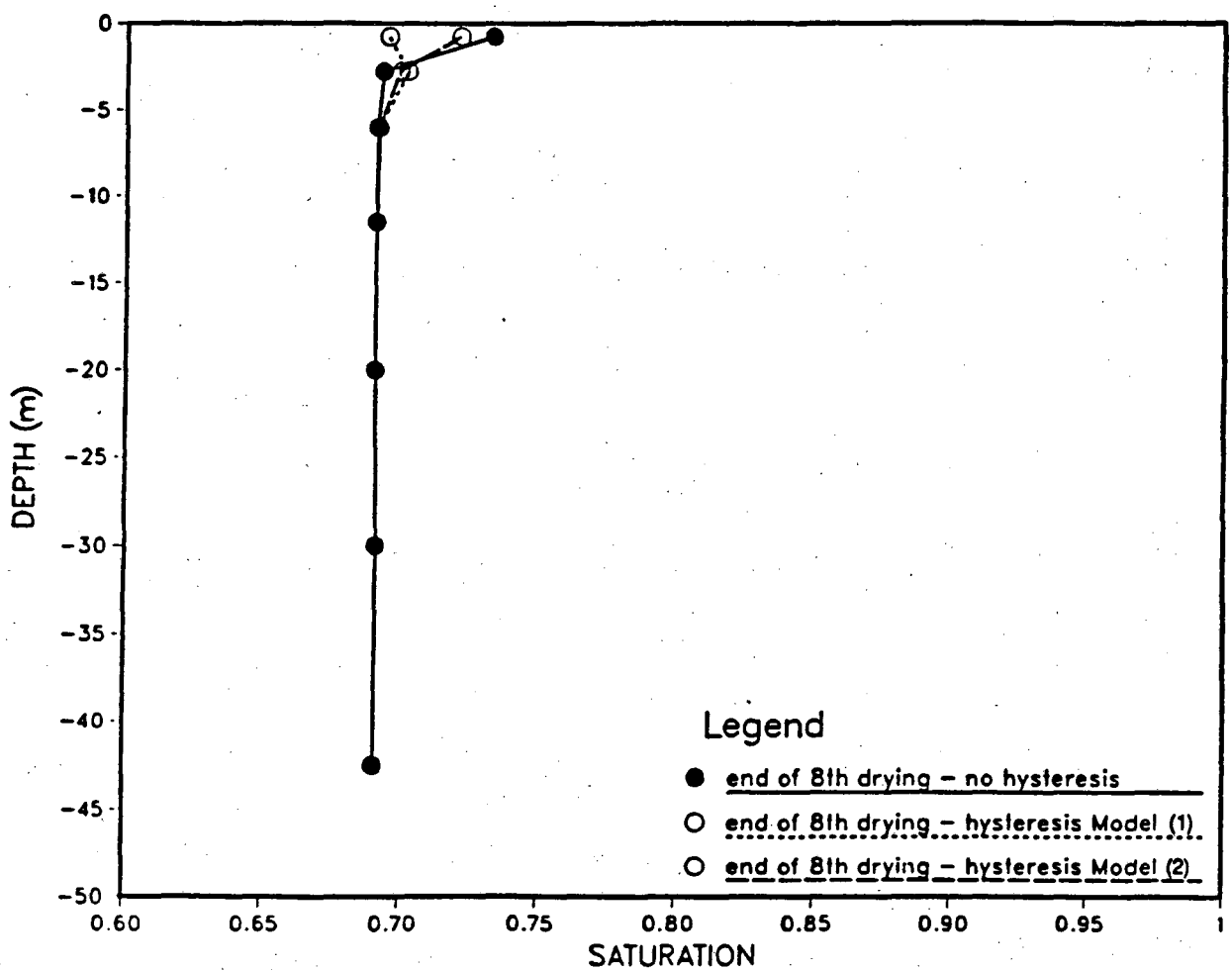

Figure 23a. One year wetting/drying cycle: Simulated liquid saturations for the matrix cross section at 0.5 mm distance from the fracture.

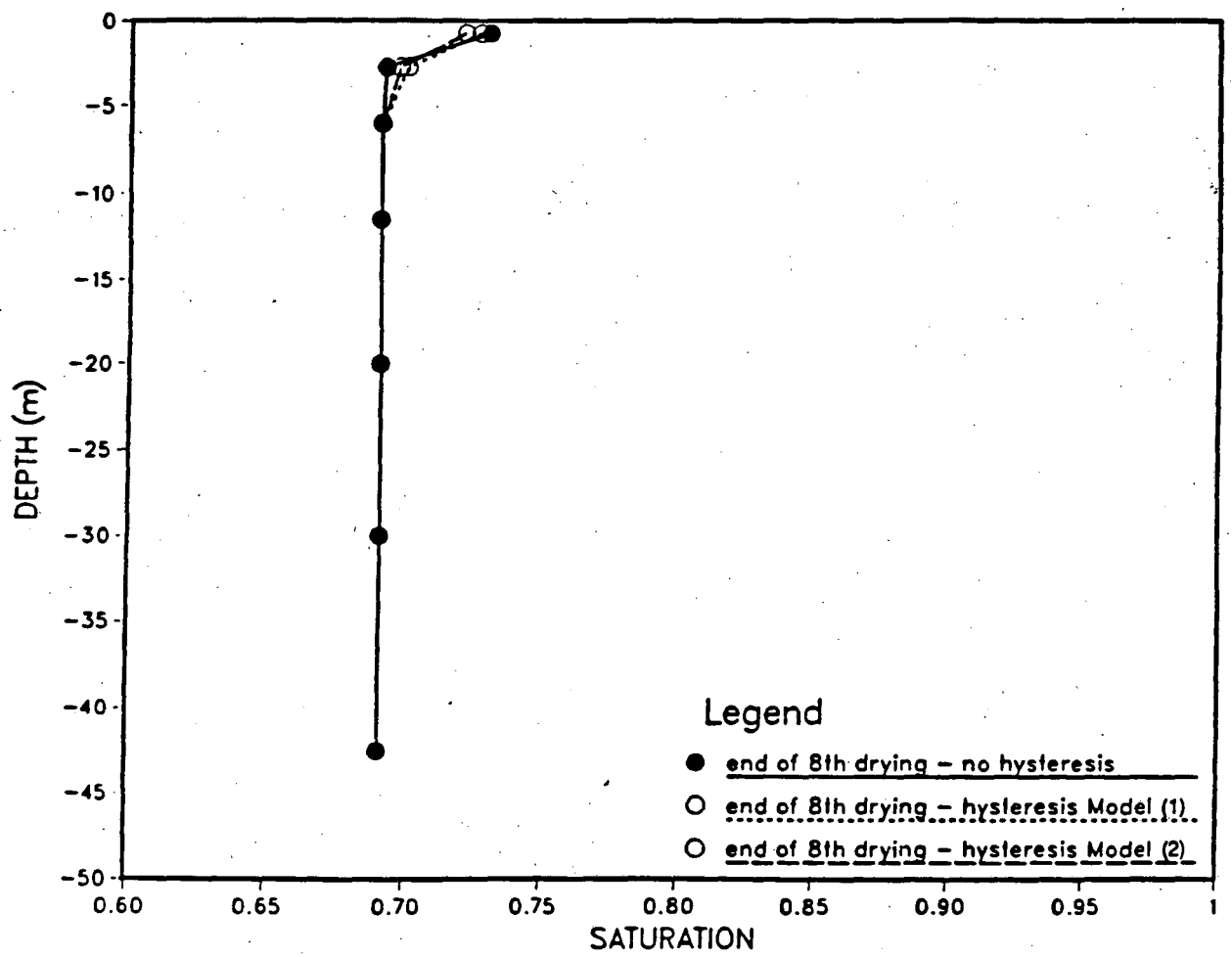

Figure 23b. One year wetting/drying cycle: Simulated liquid saturations for the matrix cross section in the center of the matrix.

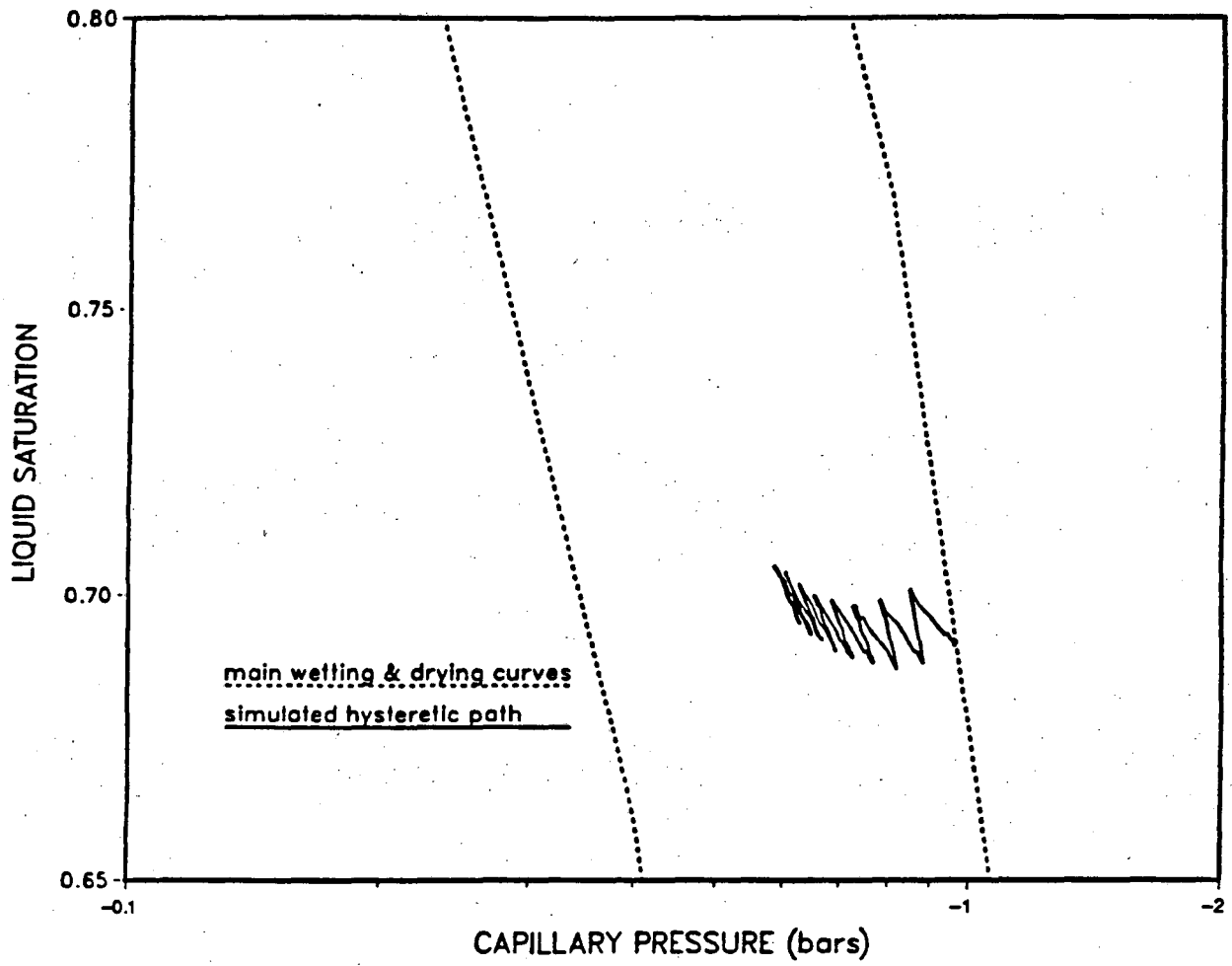

Figure 24a. One year wetting/drying cycle: Simulated hysteretic path at 0.5 mm distance from the fracture and 0.75 m depth with model (1).

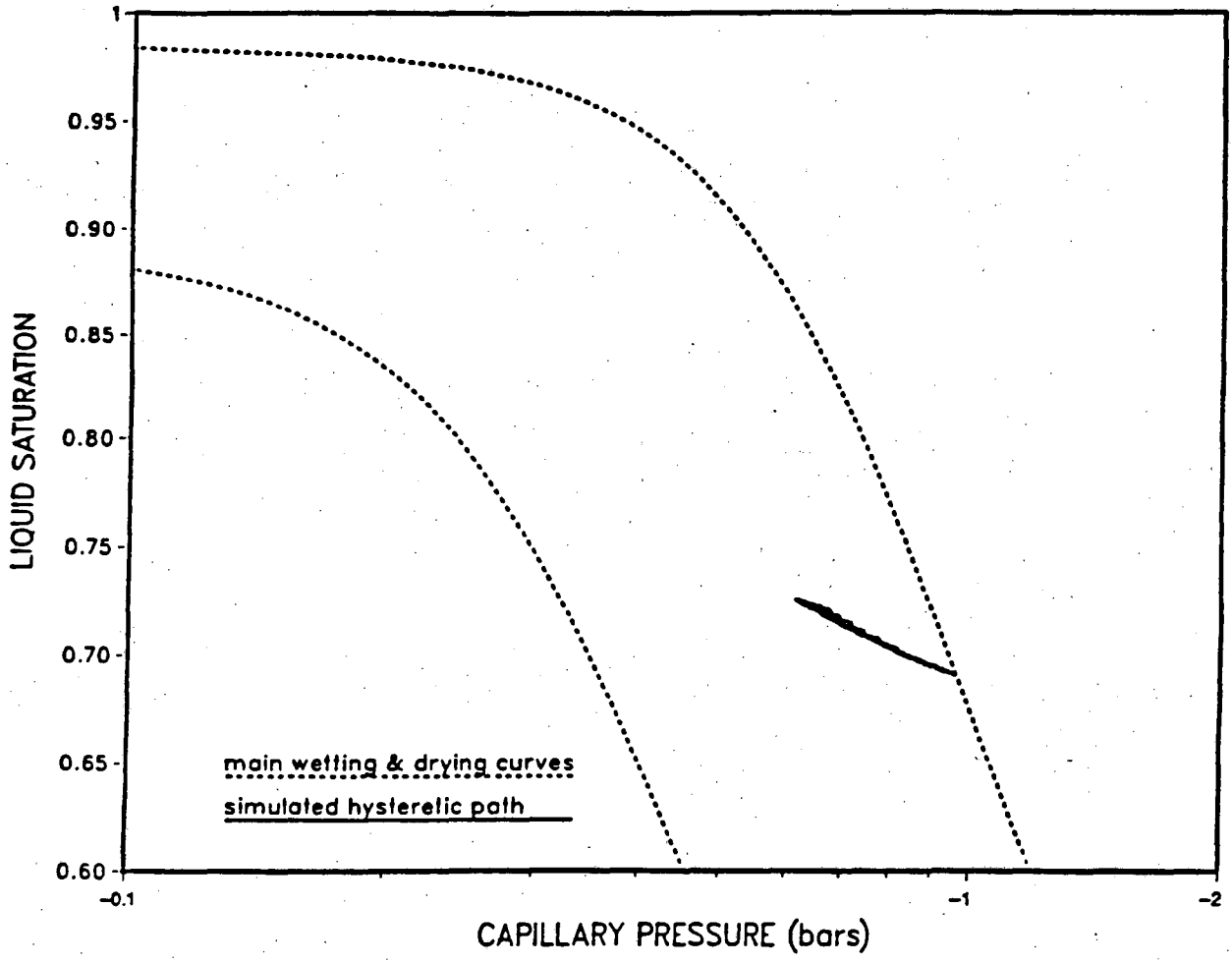

Figure 24b. One year wetting/drying cycle: Simulated hysteretic path at 0.5 mm distance from the fracture and 0.75 m depth with model (2).

6.0. SUMMARY AND CONCLUSIONS

Based on capillary hysteresis models reported in the literature, three hysteresis models have been developed and incorporated into a numerical simulator for unsaturated flow. In these three models different principles are used for determining the scanning paths: in model (1) the scanning paths are interpolated from tabulated first-order curves, in model (2) simple interpolation functions are used for scaling the scanning paths from the expressions of the main wetting and main drying curves and in model (3) the scanning paths are determined from expressions derived based on the dependent domain theory of hysteresis.

Using the three models preliminary simulations have been carried out in order to test the performance of the models as well as to obtain first-order estimates of the possible hysteresis effects in the welded units at Yucca Mountain, given the limitations of presently available data. An idealized fracture-rock matrix system with material properties reported for the welded units at Yucca Mountain by Rulon et al. (1986) was simulated under variable infiltration conditions. The width of the hysteresis envelope was estimated based on experimental results from soil literature, by assigning a ratio of $\alpha_{wetting}/\alpha_{drying} \approx 2$ and the comparisons were made between the hysteretic cases and the non-hysteretic case that took place along the main drying curve alone. The following hysteretic effects were observed:

1. Due to the lower matrix capillary suction and lower matrix liquid relative permeabilities, pulse in the fracture penetrated deeper in the hysteretic case than in the non-hysteretic case.

2. Due to the combined effect of lower matrix capillary suction and higher fracture flow, the matrix liquid saturation distribution had a more smeared shape in the hysteretic cases. In the non-hysteretic case with higher matrix suctions the

excess water from the fractures was absorbed into the matrix more rapidly and S-shaped matrix liquid saturation distributions resulted.

3. Strong hysteretic behavior was limited to the uppermost one or two layers (0.25 – 0.75 m depth). In these layers non-uniform liquid saturation distributions resulted even after capillary pressure equilibrium with the adjacent fracture was reached.

4. Using a theoretically derived hysteresis model, model (3), and assuming that the main wetting and drying curves converge towards the same maximum saturation, the pulse in the fracture penetrated ≈ 1 m deeper in the hysteretic case. The biggest local difference in matrix liquid saturations between the hysteretic and the non-hysteretic cases at the end of the simulations was ≈ 4%.

5. With the two other models the hysteresis effects were somewhat bigger. Since the derivation of these models is empirical, experimental scanning curve data should be available for their calibration before quantitative estimates are made based on their results. The observed increase in the hysteresis effects is, however, likely to be in part a result of the fact that a different main wetting curve was used. The "slight pumping" effects observed with model (1) also increased the hysteresis effects somewhat.

Based on the simulations carried out conclusions about the performance of the various models as well as some recommendations for their future use can also be made.

1. **Model (1)**

   Due to pronounced pumping effects model (1) failed to represent the hysteresis effects in the case of the one-year pulse cycle. With a larger pulse and 10-year cycle the pumping effects were not significant and the results obtained were in reasonable agreement with those obtained with other models.

   The main advantage of this model is that any kind of measured hysteresis data can be readily incorporated and accurately modeled up to first-order scanning.

Due to the potential "pumping" effects, we do not recommend the use of this model for systems with multiple reversals unless one can be certain that pumping is not generating significant errors.

2. **Model (2)**

Due to the simplifying assumption, that after a reversal from a second-order curve the process returns back to the original first-order curve, discontinuities in the scanning paths are present. In one of the cases this generated serious numerical solution convergence problems. These problems can be avoided by incorporating the computation of third- and higher-order scanning curves in a manner similar to that used for model (3) (a linear approximation is used between the latest point of the reversal and the proper point of convergence).

If measured scanning curve data is available it can be incorporated into this model by adjusting the curvature coefficient ε. No pumping can take place with this model.

3. **Model (3)**

If estimates of hysteresis effects need to be made without measured scanning curve data, use of model (3) is probably most justified since the derivation of this model is based on the theory of hysteresis rather than empirical results. The design of the model allows simulations with multiple reversals to be carried out without generating pumping errors or encountering convergence problems.

Kool, J. B. and Parker, J. C., 1987. Development and evaluation of closed-form expressions for hysteretic soil hydraulic properties, *Water Resources Research, 23,* (1) 105-114 (NNA910108.0005).

Lees, S. J. and Watson, K. K., 1975. The use of a dependent domain model of hysteresis in numerical soil water studies, *Water Resources Research, 11,* (6) 943-948 (NNA.910506.013).

Montazer, P. and Wilson, W. E., 1984. Conceptual hydrologic model of flow in the unsaturated zone, Yucca Mountain, Nevada, U. S. Geological Survey Water Resources Investigation Report 84-4345, 55 pp. (NNA.870519.0109).

Mualem, Y., 1974. A conceptual model of hysteresis, *Water Resources Research, 10,* (3) 514-520 (NNA.910506.0138).

Mualem, Y., 1976. Hysteretical models for prediction of the hydraulic conductivity of unsaturated porous media, *Water Resources Research, 12,* (6) 1248-1254 (NNA.910506.0139).

Mualem, Y., 1977. Extension of the similarity hypothesis used for modeling the soil water characteristics, *Water Resources Research, 13,* (4) 773-780 (NNA.910506.0140).

Mualem, Y., 1984. A modified dependent domain theory of hysteresis, *Soil Science, 137,* (5) 283-291 (NNA.910506.0141).

Mualem, Y. and Dagan, G., 1975. A dependent domain model of capillary hysteresis, *Water Resources Research, 11,* (3) 452-460 (NNA.910506.0142).

Niemi, A., and Bodvarsson, G. S., 1987. Capillary hysteresis model HYSTR - User's Guide, Lawrence Berkeley Laboratory Report LBL-23591, Berkeley, CA, 21 pp. (NAA.910719.0005).

Niemi, A., Bodvarsson, G. S. and Pruess, K., 1987. Incorporation of the capillary hysteresis model HYSTR into the numerical code TOUGH, Lawrence Berkeley Laboratory Report LBL-23592, Berkeley, CA, 15 pp. (NAA.910719.0006).

Parker, J. C. and Lenhard, R. J., 1988. A model for hysteretic constitutive relations governing multiphase flow, 1. Saturation-pressure relations, Submitted for publication to *Water Resources Research, 23,* (12) 7817-2196 (NNA.920219.0009).

Perrens, S. J. and Watson, K. K., 1977. Numerical analysis of two-dimensional infiltration and redistribution, *Water Resources Research, 13,* (4) 781-790 (NNA.910506.0143).

Pickens, J. F. and Gillham, R. W., 1980. Finite element analysis of solute transport under hysteretic unsaturated flow conditions, *Water Resources Research, 16,* (6) 1071-1078 (NNA.910506.0144).

Poulovassilis, A., 1962. Hysteresis of pore water: an application of the concept of independent domains, *Soil Science, 90,* 405-412 (NNA.910506.0145).

Poulovassilis, A. and Childs, E.C., 1971. The hysteresis of pore water: the nonindependence of domains (1971), *Soil Science, 112,* 301-312 (NNA.910506.0146).

Poulovassilis, A. and Tzimas, E., 1975. The hysteresis in the relationship between hydraulic conductivity and soil water content, *Soil Science, 120,* (5) 327-331 (NNA.910506.0147).

7.0. REFERENCES

Aggelides, S. and Youngs, E. G., 1978. The dependence of the parameters in the Green and Ampt infiltration equation on the initial water content in draining and wetting states, *Water Resources Research, 14,* (5) 857-862 (NNA.910506.0130).

Banerjee, M. and Watson, K. K., 1984. Numerical analysis of soil water movement under conditions of rapid intermittency of water application, *Water Resources Research, 20,* (1) 119-125 (NNA.910108.0002).

Beven, K. and Germann, P., 1982. Macropores and water flow in soils, *Water Resources Research, 18,* (5) 1311-1325 (NNA.890327.0050).

Cary, J. W., 1975. Soil water hysteresis: temperature and pressure effects, *Soil Science, 120,* (4) 308-311 (NAA.910506.0131).

Curtis, A. A., 1977. The effects of the air phase on water movement in unsaturated porous materials, Ph.D. Thesis, Univ. of New South Wales, Sydney, Australia (NAA.910506.0132).

Curtis, A. A. and Watson, K. K., 1984. Hysteresis affected water movement in scale heterogeneous profiles, *Water Resources Research, 20,* (6) 719-726 (NAA.910506.0133).

Daily, W., Lin, W. and Buscheck, T., 1987. Hydrological properties of Topopah Springs Tuff, submitted for publication in *Journal Geophysical Research* (NAA.900123.0064).

Dane, J. H. and Wierenga, P. J., 1975. Effect of hysteresis on the prediction of infiltration, redistribution and drainage of water in layered soil, *Journal of Hydrology, 25,* 229-242 (NNA.910506.0134).

Gillham, R. W., Klute, A. and Heermann, D. F., 1976. Hydraulic properties of a porous medium: measurement and empirical representation, *Soil Science Society America Journal, 40,* 203-207 (NNA.890522.0231).

Hoa, N. T., Gaudy, R. and Thirrot, C., 1977. Influence of the hysteresis effect on transient flows in saturated-unsaturated porous media, *Water Resources Research, 13,* (6) 992-996 (NNA.910506.0135).

Jaynes, D. B., 1984. Comparison of soil water hysteresis models, *Journal Hydrology, 75,* 287-299 (NNA.910108.0003).

Killough, J. E., 1976. Reservoir simulation with history dependent saturation functions, *Society of Petroleum Engineering Journal, 16,* (1) 37-48 (NNA.910506.0136).

Klavetter, E. A. and Peters, R. R., 1986. Fluid flow in a fractured rock mass, Report SAND85-0855, Sandia National Laboratory, Albuquerque, NM, 55 pp. (NNA.870721.0004).

Klute, A. and Heermann, D. F., 1974. Soil water profile development under a periodic boundary condition, *Soil Science, 117,* (5) 265-271 (NNA.910108.0004).

NOTE: Parenthesized numbers following each cited reference are for U. S. Department of Energy OCRWM Records Management purposes only and should not be used when ordering the publication.

Pruess, K., 1983. GMINC-a mesh generation for flow simulations in fractured reservoirs, Lawrence Berkeley Laboratory Report LBL-15227, Berkeley, CA, 64 pp. (NNA.910307.0134).

Pruess, K., 1986. TOUGH-users guide, Lawrence Berkeley Laboratory Report LBL-20700, Berkeley, CA, 84 pp. (NNA.890315.0010).

Rulon, J., Bodvarsson, G. S. and Montazer, P., 1986. Preliminary numerical simulations of groundwater flow in the unsaturated zone, Yucca Mountain, Nevada, Lawrence Berkeley Laboratory Report LBL-20553, Berkeley, CA, 88 pp. (NNA.87908.0027).

Scott, P. S., Faraquhar, G. J. and Kouwen, N., 1983. Hysteretic effects on net infiltration, Proceedings of "National Conference on Advances in Infiltration," Chicago, IL (NNA.910506.0148).

Topp, G. C., 1969. Soil water hysteresis measured in a sandy loam and compared with the hysteretic domain model, *Soil Science Society America Proceedings, 33,* 645-651 (NNA.910506.0149).

Topp, G. C., 1971. Soil water hysteresis in silt loam and clay loam soils, *Water Resources Research, 7,* (4) 914-920 (NNA.910506.0150).

Topp, G. C. and Miller, E. E., 1966. Hysteretic moisture characteristics and hydraulic conductivities of glass-bead media, *Proceedings Soil Science Society America, 30,* 156-162 (NNA.910506.0151).

Vachaud, G. and Thony, J. L., 1971. Hysteresis during infiltration and redistribution in a soil column at different initial water contents, *Water Resources Research, 7,* (1) 111-127 (NNA.910506.0152).

van Genuchten, M. T., 1980. A closed-form equation for predicting the hydraulic conductivity of unsaturated soils, *Soil Science Society America Journal, 44,* 892-898 (NNA.890522.0287).

Wang, J. S. Y. and Narasimhan, T. N., 1985. Hydrological mechanisms governing fluid flow in a partially saturated, fractured, porous medium, *Water Resources Research, 21,* (12) 1861-1874 (NNA-891109.0050).

Wang, J. S. and Narasimhan, T. N., 1986. Hydrologic mechanics governing partially saturated fluid flow in fractured welded units and porous non-welded units at Yucca Mountain, Report SAND85-7114, LBL-21022, Sandia National Laboratory, Albuquerque, NM (NNA.870806.0063).

Watson, K. K. and Perrens, S. J., 1973. Numerical analysis of intermittent infiltration redistribution, paper presented at Hydrology Symposium, Inst. Eng. Aust., Perth, West Australia (NNA.910506.0155).

Whisler, F. D. and Watson, K. K., 1969. Analysis of infiltration into draining porous media. *Journal Irrigation Drainage, Division American Society of Civil Engineers, 95,* (4) 481-491 (NNA.910506.0156).

Witherspoon, P. A., Wang, J. S. Y., Iwai, K. and Gale J. E., 1980. Validity of cubic law for fluid flow in a deformable rock fracture, *Water Resources Research, 16,* (6) 1016-1027 (NNA.891109.0039).

The following number is for U. S. Department of Energy OCRWM Records Management purposes only and should not be used when ordering this publication: NNA.910719.001.

LAWRENCE BERKELEY LABORATORY
UNIVERSITY OF CALIFORNIA
TECHNICAL INFORMATION DEPARTMENT
BERKELEY, CALIFORNIA 94720